MICROSTRUCTURAL ANALYSIS OF HELIUM DISTRIBUTION IN NICKEL AND INCONEL X750

A Thesis Submitted to the College of

Graduate Studies and Research

In Partial Fulfillment of the Requirements

For the Degree of Master of Science

In the Department of Mechanical Engineering

University of Saskatchewan

Saskatoon

By

Aseem Kirtiman Chauhan

PERMISSION TO USE

In presenting this thesis in partial fulfillment of the requirements for a Postgraduate degree from the University of Saskatchewan, I agree that the Libraries of this University may make it freely available for inspection. I further agree that permission for copying of this thesis in any manner, in whole or in part, for scholarly purposes may be granted by Prof. Jerzy A. Szpunar, the Professor who supervised my thesis work or in his absence, by the Head of the Department or the Dean of the College, in which my thesis work was done. It is understood that any copying or publication or use of this thesis or parts thereof for financial gain shall not be allowed without my written permission. It is also understood that due recognition shall be given to me and to the University of Saskatchewan in any scholarly use which may be made of any material from my thesis.

Requests for permission to copy or to make other uses of materials in this thesis in whole or part should be addressed to:

Head of the Department of Mechanical Engineering
University of Saskatchewan
57 Campus Drive
Saskatoon, Saskatchewan S7N 5A9
Canada

OR

Dean

College of Graduate Studies and Research

University of Saskatchewan
107 Administration Place
Saskatoon, Saskatchewan S7N 5A2
Canada

ABSTRACT

Nickel alloys have found ever increasing use in the nuclear sector in recent times. Inconel X750 and other nickel-based alloys are used in the construction of reactor fuel channels. Thermal neutrons cause transmutation of nickel, and the nuclear reactions that take place within some nuclear reactor components result in the production of helium. Helium accumulation causes the swelling, reduces material strength and finally leads to failure. This project addresses two impact areas, viz., i) improving safety of nuclear energy systems and, ii) advancing knowledge on nuclear materials used in CANDU (Canada Deuterium Uranium) reactors.

The project discusses the experiments carried out on helium irradiated pure Ni and Inconel X750 alloy in order to understand void formation due to helium. SEM (Scanning Electron Microscope) and TEM (Transmission Electron Microscopy) analyses were carried out to establish a relationship between helium void formation and temperature. In addition, EBSD (Electron Backscattered Diffractometry) analysis was carried out to analyse the concentration of helium voids at various grain boundaries.

The project explains in detail the use of SPECTER code to calculate the gas production levels and DPA (displacement per atom) and SRIM (Stopping and Range of Ions in Matter) software, which was used to carry out the various calculations necessary to perform helium ion implantation experiments. As it was difficult to work with irriadted materials from the reactor on account of safety concerns, and also cost associated with working with heavily irradiated materials, the method of helium ion implantation was adopted for this project.

Results showed that at higher temperatures both irradiated pure Ni and Inconel X750 alloy showed accumulation of voids towards the grain boundaries. TEM and EDS (Energy Dispersive Spectroscopy) analysis on irradiated pure Ni confirmed the presence of voids near the grain boundaries.

A statistical relationship was also established between the accumulation of voids and the grain boundary misorientation. It was found out that for both irradiated pure Ni and Inconel X750 alloy the concentration of voids increased with an increase in the grain boundary misorientation. This was due to more free volume available at higher angle grain boundaries.

PREFACE

Sections of this thesis have been submitted as multi-authored papers and abstracts in various conferences. The results in this study were presented at National and International Conferences.

1. M. Singh, L. Malakkal, A.K Chauhan. J.A. Szpunar, M.P. Bradley and M. Chicoine, Effects of irradiation o thermal conductivity of nickel alloys, The Nuclear Materials Conference, Montpellier, France, November 7-10, 2016

2. A.K. Chauhan, J.A. Szpunar, B. Szpunar, M.P. Bradley, V.K. Saini, M. Griffiths and M. Chicoine, Helium based degradation of Nickel Superalloys, 3rd International Conference on Manufacturing Engineering and Technology for Manufacturing Growth, Vancouver, Canada, August 1-2, 2015. ISBN: 978-1-61275-074-3, IERI & PRESS, 178-181.

3. A.K. Chauhan, J.A. Szpunar and M. Chicoine, Microstructural Characterization of Nickel Superalloys for CANDU nuclear reactors, The Nuclear Materials Conference, Clearwater Beach, Florida, October 27-30, 2014

4. A.K. Chauhan and J.A. Szpunar, Microstructural Characterization of Nickel Superalloys for CANDU nuclear reactors, 26th Canadian Materials Science Conference, Saskatoon, Saskatchewan, June 1-4, 2014

ACKNOWLEDGMENTS

I would like to express my sincere gratitude to my supervisor, Prof. Jerzy A. Szpunar for his constant guidance and support. I thank Prof.Szpunar for his supervision, good advice, support and friendship that has been invaluable on both academic and personal level. The contributions of Prof. Akindele Odeshi and Dr. Michael P. Bradley, my advisory committee members are greatly appreciated. I am very grateful to Dr. M. Bradley and Dr. Barbara Szpunar for helping me to use the implantation software and for helping me to understand the implantation physics and technique.

I would also like to thank Mr. Martin Chicoine for carrying out the ion implantations at the University of Montreal, and to Dr. B. S. Amirkhiz for carrying out the TEM analysis. The support of Mr. Nan Fang Zhao in my experimental investigations is also appreciated.

Dr. Salman Razavi is greatly appreciated for the time spent in ensuring my sound knowledge of texture of materials and for teaching me how to use the various facilities in the lab. I would also like to thank the members of my research group for their constant help and support.

My sincerest thanks go to my dearest Mom, Dad and elder brother for their heartwarming love and encouragement throughout all of my university studies.

DEDICATION

sarva-dharman parityajya
mam ekam saranam vraja
aham tvam sarva-papebhyo
moksayisyami ma sucah

(Bhagwat Gita: Chapter 18 verse 66)

“Abandon all varieties of religion and just surrender unto Me (Lord Krishna). I shall deliver you from all sinful reaction. Do not fear.”

TABLE OF CONTENTS

LIST OF TABLES

LIST OF FIGURES

LIST OF ABBREVIATIONS AND SYMBOLS

ABBREVIATIONS

NASA	National Aeronautics and Space Administration
IPCC	Intergovernmental Panel on Climate Change
IEA	International Energy Agency
CANDU	Canada Deuterium Uranium
AECL	Atomic Energy of Canada Limited
PHWR	Pressurized Heavy Water Reactor
SEM	Scanning Electron Microscope/microscopy
DPA	Displacement per atom
SRIM	Stopping and Range of Ions in Matter
EBSD	Electron Backscattered Diffractometry
TEM	Transmission Electron Microscopy
FIB	Focused Ion Beam
EDS	Energy Dispersive Spectroscopy
EAM	Embedded-atom method
MD	Molecular dynamics
FEI	Field Electron and Ion

SYMBOLS

^{o}C	Degree Celsius
^{o}F	Degree Fahrenheit
keV	Kilo-electron volt
amu	Atomic mass unit
Å	Ångström
μA	Microampere
appm	Atomic parts per million

CHAPTER ONE

INTRODUCTION

1.1 Overview

Global Warming is one of the most serious and challenging problems faced in the 21st century. According to the National Aeronautics and Space Administration (NASA) earth's average temperature has increased by one degree celsius during the last century. The Intergovernmental Panel on Climate Change (IPCC) has forecasted a further temperature rise of 2.5 – 10°C for the next century. Global warming has some very serious and devastating environmental repercussions like rising sea level, melting of glaciers and coastal flooding, intense heat waves, changing weather patterns, irreversible damage to biodiversity (plant and animal life), destruction of the coral reefs and many more [1]. Emission of greenhouse gases and rampant deforestation are two major contributory causes of global warming. According to International Energy Agency (IEA) 2010 Report (World Energy Outlook), there has been a 75% increase of global energy consumption over a period of 35 years (1973 – 2008). According to IEA the global CO_2 emissions rose by 4.6% in 2010 which is an increase of nearly 1.3Gt CO_2 [2].

Problems like environmental deterioration, climate change and increasing CO_2 emissions are urgent challenges which need to be taken care of in the current century itself. In order to tackle all these problems some very fundamental, ecologically and economically viable as well as environmentally sustainable alternatives for energy generation are needed, especially when most of the CO_2 emissions are contributed by the energy sector.

As per the predictions in the United Nations reports, the world population would be around 8.7 billion by 2035, thereby substantially increasing the demand for energy. In the current scenario more than 70% of the energy demand comes from developing nations like India and China. China overtook United States as the top CO_2 emitter in the year 2007. So there is urgent need to switch to less polluting, more reliable and more efficient ways of energy generation like the nuclear energy [3].

According to the World Energy Outlook Report (2006 edition) nuclear energy would play a major role in reducing CO_2 emissions. It is also a cost-effective alternative on account of abundant availability of nuclear fuel [3].

Nuclear energy has various advantages over conventional fuels. Its usage would lead to a decrease in the greenhouse gas emissions and it is considered to be extremely efficient and reliable. Thus our environmental compulsions prompt us to shift to nuclear power and allocate more funds for making nuclear power cheaper and safer for the future.

Saskatchewan is one of world's main exporters of uranium, a nuclear fuel used for power generation. In 2013, Canada produced 9,331.5 tonnes of uranium from the mines in Northern Saskatchewan [4]. This research supports development of materials with improvement in performance in operating nuclear reactors. Safety, efficiency, economy, waste minimization and fuel burn-up are the most significant areas that need to be studied and improved upon. These improvements are considered imperative for next generation of innovative energy systems known as Gen IV nuclear reactors. Among many components, Nickel is peerlessly a metal that is used to make superior class of materials with good mechanical strength at high temperatures. Possessing such properties, these alloys have various industrial applications. On account of their good corrosion characteristics, these are used extensively in turbine engines. The use of nickel alloys have marked their significant presence in nuclear reactors too. In power reactors, these super alloys (in a neutron flux environment) tend to absorb the thermal neutrons. Nickel super alloys are being used as garter springs and spacers in the core of CANDU (Canada Deuterium Uranium) nuclear reactors. But they tend to fail over a period of time thus raising concerns for the safety of nuclear reactors.

1.2 Motivation

Nickel super-alloy Inconel X750 has good creep properties and good mechanical strength at high temperatures thus making it an ideal candidate for structural components within reactor cores. Inconel X750 contains approximately 70 wt% Ni [5, 6]. Inconel X750 is used as garter springs (also known as spacers) in CANDU reactors to maintain a gap between the pressure tube and the calandria tube. The limitation with using Inconel X750 spacers is that CANDU reactors have extremely high thermal neutron flux spectra, which combined with the high thermal neutron

cross section of ^{58}Ni present in the alloy, results in radiation damage and production of hydrogen and helium [6]. This internal production of hydrogen and helium leads to the formation of gas cavities which reduces mechanical strength and finally leads to failure. Previous studies on ex-service garter springs have shown that helium voids are usually accumulated towards the grain boundary of the Inconel X750 alloy [6]. However, there is no sufficient information regarding the role of microstructure, texture and grain-boundary structure that effects the diffusion of helium and formation of helium-void complexes.

The effect of grain boundary structure on the accumulation of voids from material irradiated in a power reactor has not been studied before. In order to understand the relationship between helium voids and grain boundary structure, the method of helium ion implantation was adopted. This was imperative as it is difficult to work with ex-service material because of safety concerns and cost associated with working with heavily radioactive materials.

1.3 Research objectives

- To optimize the method of helium implantation and analysis of bubble formation in pure Ni and Inconel X750.
- To establish a relationship between temperature and the formation of voids in pure Ni and Inconel X750.
- To elucidate the influence of grain boundary structure on the concentration of voids in pure Ni and Inconel X750.

1.4 Thesis arrangement

The current chapter of the thesis consists of the motivation and objectives of this M.Sc. Research Project. Chapter two consists of literature review and previous research on pure Ni and Inconel X750 alloy. Relevant information on materials investigated and experimental techniques are outlined in chapter three, while chapter four contains results, their analysis and discussion. Conclusions drawn from the research are presented in chapter five.

CHAPTER TWO

LITERATURE REVIEW

2.1 CANDU Reactor

CANDU reactors were first developed in the late 1950s and 1960s in Canada by a partnership between AECL (Atomic Energy of Canada Limited), Ontario Power Generation, GE Canada, and other companies. CANDU reactors are also operative in India, Pakistan, Argentina, South Korea, Romania and China [6, 7]. It is a Canadian designed power reactor of PHWR (Pressurized Heavy Water Reactor) type. CANDU reactors are considered as one of the most efficient of all reactors using Uranium, for this type of a reactor does not need a uranium enrichment facility and even fuel reprocessing is not required. As a result the operating costs are substantially low. This reactor uses heavy water (deuterium oxide) as a moderator. The advantage of using heavy water is that it is easily available, can be re-used and on account of its low neutron absorption rate, is extremely efficient. A CANDU reactor core comprises of small diameter of fuel channels rather than one large pressure vessel. The pressure tubes present inside the fuel channel consist of moveable fuel bundles which allow maximum burn-up of all the fuel in the reactor core. Many components of the CANDU reactor core are moveable and accessible for repairs, thus improving the life expectancy of the reactor core [7]. Figure 2.1 gives an overall idea of a CANDU nuclear reactor.

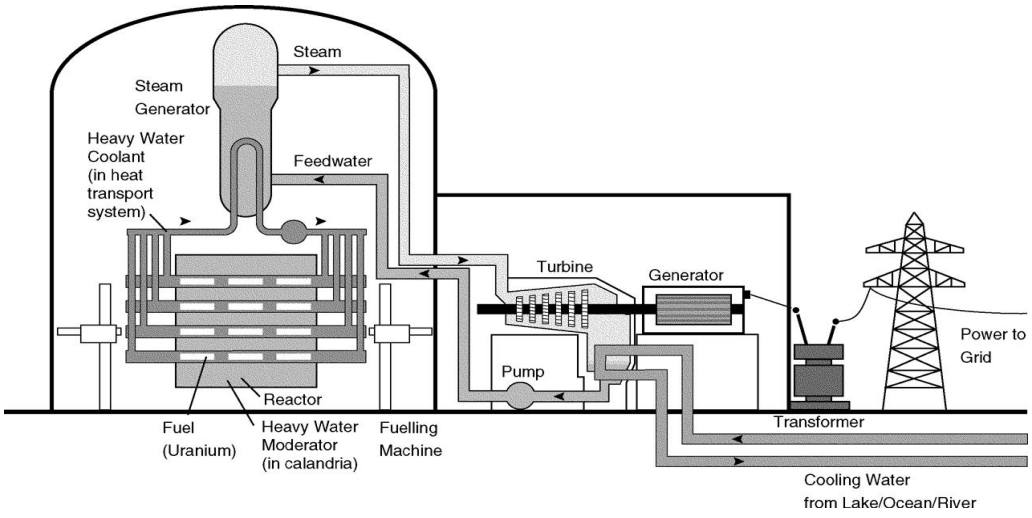

Figure 2.1: CANDU reactor schematic [8].

Currently there are 19 operating CANDU reactors in Canada with a net capacity of 13,513MWe [9].

2.2 Fuel Channel Assembly

The fuel channel assembly of a CANDU reactor consists of zirconium-niobium alloy Zr-2.5wt%Nb pressure tubes which are centered in calandria tubes made of zirconium alloy. These pressure tubes are expanded into stainless steel end fittings at each end. The pressure tubes are thermally insulated from the moderator by the annulus gas (such as CO_2) between the pressure tube and the calandria tube. The pressure tube contains the fuel bundles and the heavy water moderator is present outside the calandria tubes. The annulus gas prevents the heat flow from the high pressure coolant in the pressure tube to the moderator. The heat loss to the moderator would result in a loss of heat efficiency as less heat would be carried to the steam generators [10]. Inconel X750 spacers positioned along the length of the pressure tube maintain an insulating gas gap and prevent contact between the two tubes. Each end fitting consists of a fuel support plug, channel closure and a liner tube [11]. A detailed view of a fuel channel assembly can be seen in figure 2.2.

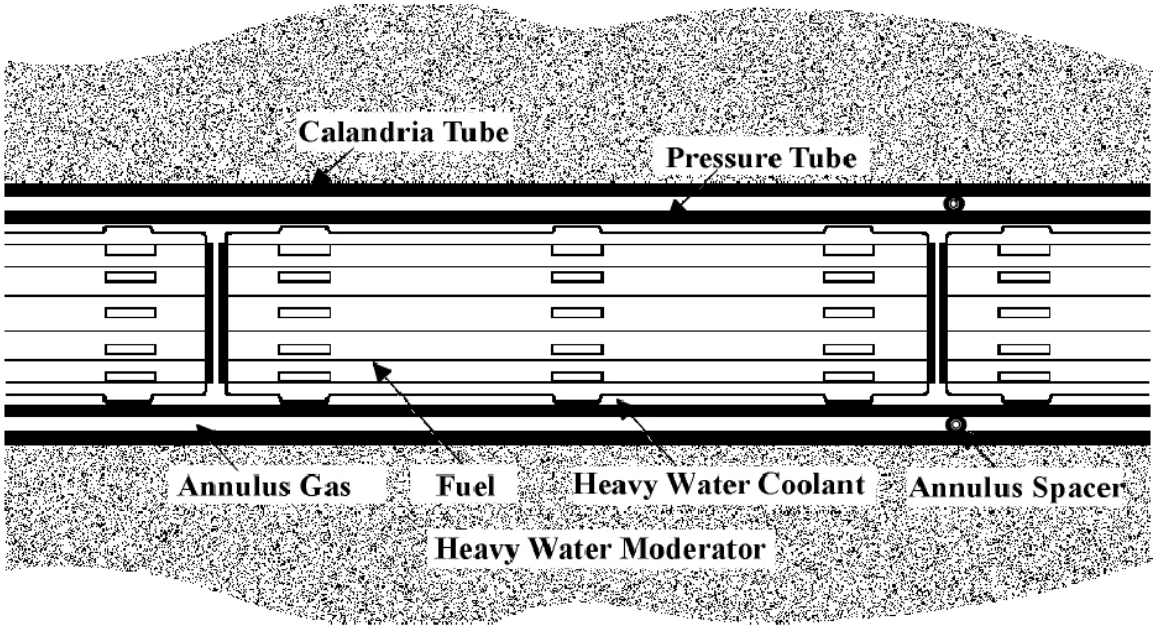

Figure 2.2: CANDU Fuel Channel Arrangement [12].

CANDU reactors are designed for a target life of around 60 years which could be further expanded by the replacement of fuel channels. It is the Inconel X750 spacers present in the fuel channel assembly which cause failure of these fuel channels and need to be replaced and serviced periodically [11].

2.3 Inconel X750 in CANDU reactors

Inconel X750 is a precipitation hardened nickel super-alloy with high strength, corrosion resistance and resistance to creep at high temperatures. Precipitation strengthening obtained from a fine array of gamma prime, γ^1, within the γ matrix contributes to the strengthening in Ni super-alloys [13]. Precipitation hardening is a heat treatment process that leads to the formation of uniformly dispersed particles within a metal's grain structure that strength the metal by hindering dislocation motion [13]. This is done by a high temperature solution treatment followed by rapid cooling process. It is the rapid cooling which results in strengthening the metal matrix by preventing the creation and propagation of lattice defects [13].

Inconel X750 is used as garter spring- type spacers in the fuel channels of CANDU reactors to separate the pressure tubes from calandria tubes and thus maintain an insulating gas gap between the hot pressure tube (operating at 260°C - 310°C) and the cold calandria tube (operating at 60°C - 70°C). There are approximately 380 horizontal fuel channels in every CANDU reactor which consists of four spacers per channel totalling to 1520 Inconel X750 spacers per reactor. [6]. A cross sectional schematic of a CANDU fuel channel can be seen in figure 2.3 and figure 2.4.

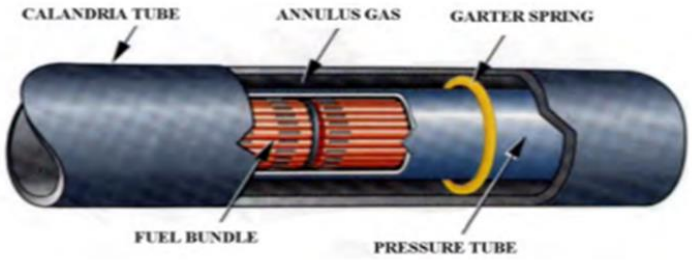

Figure 2.3: Inconel X750 spacers (garter springs) in a fuel channel of a CANDU reactor [6].

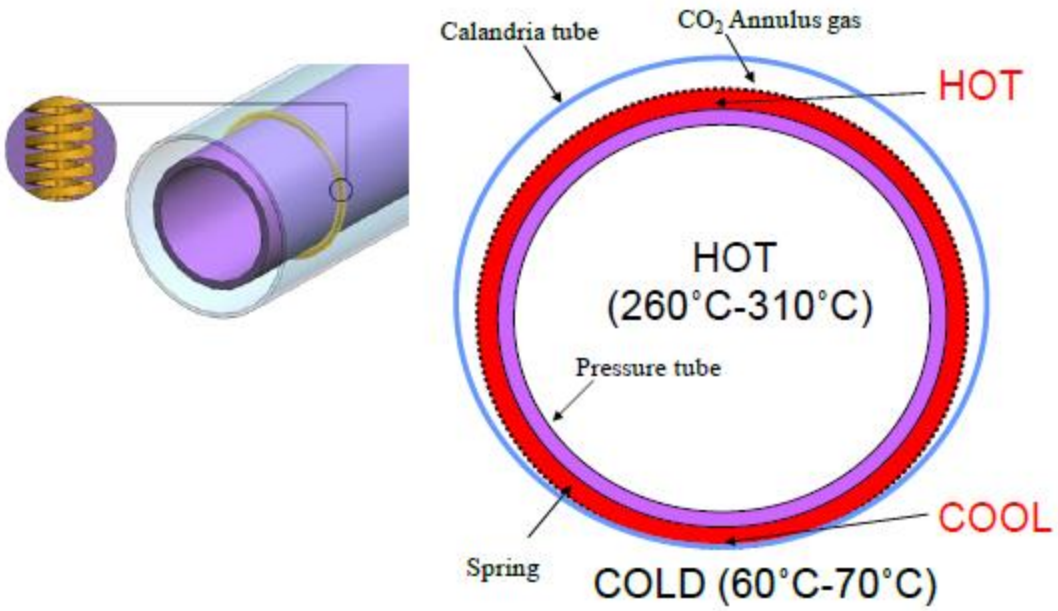

Figure 2.4: Inconel X750 spacers (garter springs) maintaining an insulating gap between the pressure tube and calandria tube [6].

Post-irradiation examination of Inconel X750 spacers removed from CANDU reactors have been done under the supervision of M. Griffiths. The examinations showed embrittlement and lower ultimate tensile strength in the irradiated materials compared to the unirradiated materials. The embrittlement was characterized by intergranular failure [6]. The reason for intergranular failure could be that more He was segregated at grain boundaries due to higher operating temperatures in the reactor core [6]. These studies even concluded that there was a higher density of cavities along the grain boundaries compared to the matrix [6]. Figure 2.5 shows the images obtained from SEM (Scanning Electron Microscope) imaging of the ex-service spacers removed from CANDU reactors.

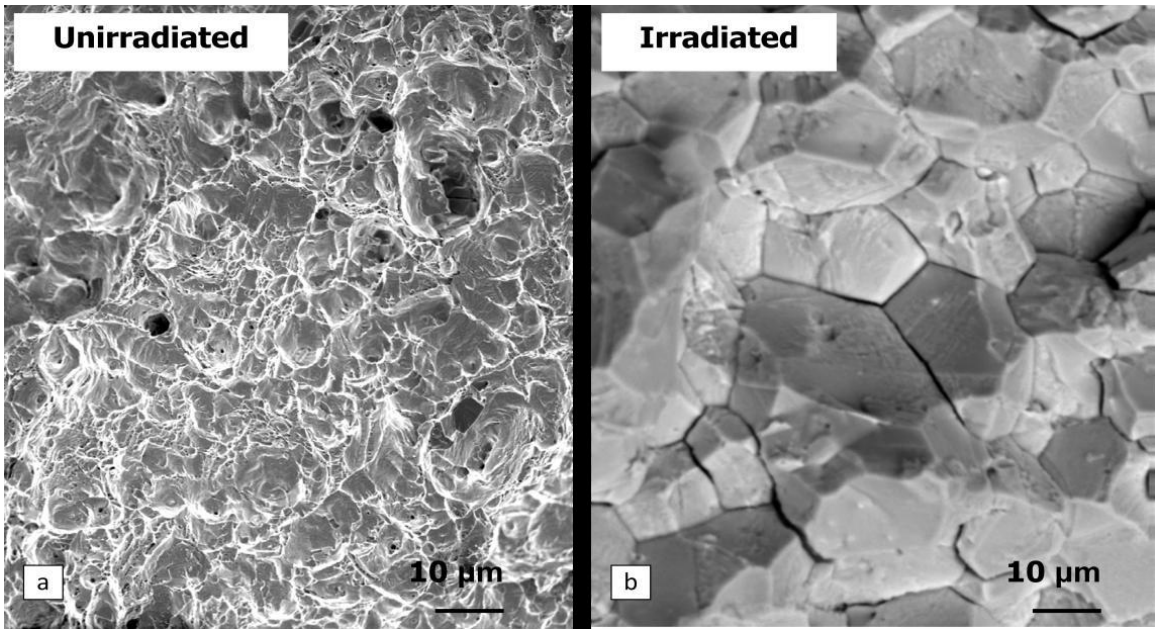

Figure 2.5: SEM images of (a) Unirradiated sample and (b) Irradiated sample [6].

Figure 2.5 compares the fracture surfaces of unirradiated and irriadiated Inconel X750 spacers. These samples were subjected to mechanical testing at room temperature. It is clearly seen that the unirradiated sample showed (a) ductile failure whereas the irradiated sample (b) showed intergranular failure which clearly indicates that the helium cavaties are accumulated more towards the grain boundaries rather than the bulk of the material [6]. These helium cavaties are formed due to the thermal neutron damage of the ^{58}Ni which is present in the Inconel X750 alloy.

2.4 Thermal Neutron Damage

Inconel X750 contains around 70 wt% Ni out of which ^{58}Ni has a concentration of approximately 68%, which is known to have a high thermal neutron cross section [6, 14].

Nickel containing components are susceptible to degradation in the reactors having high thermal and epi-thermal neutron flux. This results in a high rate of transmutation of ^{58}Ni to ^{59}Ni (which is not present in natural nickel), followed by various nuclear reactions involving ^{59}Ni. ^{59}Ni is generated by thermal neutron capture by ^{58}Ni, which is the most abundant isotope of Ni. ^{59}Ni, in turn, has high neutron cross-section for the reactions listed below [15, 16].

$$^{58}Ni + n \rightarrow {}^{59}Ni + \gamma$$

$$^{59}Ni + n \rightarrow {}^{56}Fe + {}^{4}He$$

$$^{59}Ni + n \rightarrow {}^{59}Co + H$$

$$^{59}Ni + n \rightarrow {}^{60}Ni + \gamma$$

The ^{59}Ni reactions are extremely exothermic and produces charge particles and heavy atomic recoils which lead to radiation damage [17].

CANDU reactors have a high thermal and epi-thermal neutron flux because of which the Ni superalloys undergo two-stage transmutation from ^{58}Ni to ^{59}Ni and degrade. The ^{59}Ni so generated undergoes various reactions; and as a result helium is produced, which leads to the formation of gas cavities. Helium accumulation causes swelling, changes spacer volume, reduces mechanical strength, and finally leads to failure. Post irradiated examination on ex-service Inconel X750 CANDU spacers indicated a reduced strength and ductility compared to unirradiated material [17, 28] Thus, a clear understanding of bubble formation and their relation to the mechanism of failure is of fundamental importance for any application of various nickel-based alloys in nuclear reactors.

Role of helium in Ni alloy is however, not well understood. The primary source of helium is the (n,α) reactions with the ^{58}Ni and ^{59}Ni isotopes. Thermal fluxes lead to significant helium generation over component lifetime. This helium can affect grain boundary integrity as the helium is accumulated more at the grain boundary as compared to bulk of the material thus inducing cracking which leads to failure [18, 29]. At very high temperatures and for components exposed to irradiation for a long time, helium concentrations as low as 5-10 appm (atomic parts per million) could induce grain boundary embrittlement for the structures operating under sufficiently high stresses. High temperatures are a cause of failure because it has been observed that high temperatures promote helium diffusion towards the grain boundary. It is known that the Ni alloys' ductility loss depends on alloy composition and microstructure, neutron dose, irradiation damage rate, neutron spectrum, temperature and applied stress. Molecular level Embedded Atom Method has been already used to calculate the bonding energy of helium-void complexes [19, 30], and an *ab-initio* study of helium migration and the formation energies of clusters has been published [20].

2.5 DPA and gas production analysis

V.K. Saini carried out a study under the guidance of J. Szpunar and B. Szpunar at the University of Saskatchewan, with the aim of finding out DPA (displacement per atom) and gas production levels like helium and hydrogen for pure Ni and Inconel X750.

The computer code SPECTER was used to calculate the gas production levels (helium and hydrogen) and DPA over the time period for forty years. In order to run SPECTER, a user needs to specify the neutron flux spectrum and composition of the alloy and can calculate displacement damage and gas production rates. SPECTER has been developed to provide users with spectral-averaged cross sections. Each reaction is listed separately and gas production cross sections can also be obtained. The program then converts the required master library files into the user's group structure and proceeds to spectral average of all calculated quantities. If an irradiation time is specified, the code will provide absolute displacements, gas production and other vital information. [20, 21]

Since the chemical composition of the alloys was given in weight percentage and not in the form of atomic composition, one had to divide the weight percentage per atomic mass for each component and next this result was divided by the sum of all of atoms. The calculations are based on maximum and minimum concentrations of Ni as the concentration of Ni varies in the alloy Inconel X750 from supplier to supplier.

The DPA resulting from helium and hydrogen production was calculated for the different elements present in the alloys. Table 2.1 shows the calculated data for Inconel X750 at maximum concentration of Ni.

Table 2.1: Calculated data for Inconel X750 at maximum concentration of Ni [22].

DPA	HELIUM(appm)	HYDROGEN(appm)	YEAR
2.85	503.05	156.32	1
21.38	6420.12	1433.47	5
45.73	14467.12	3138.53	10
68.17	21469.61	4669.19	15
88.79	27472.65	6033.02	20
107.84	32614.93	7253.10	25
125.55	37020.57	8350.31	30
142.10	40796.16	9342.17	35
157.65	44031.61	10246.38	40

(Estimated error ≈ 5%)

The calculated H, He and DPA as a function of time for Inconel X750 at maximum concentration of Ni is shown in Figure 2.6:

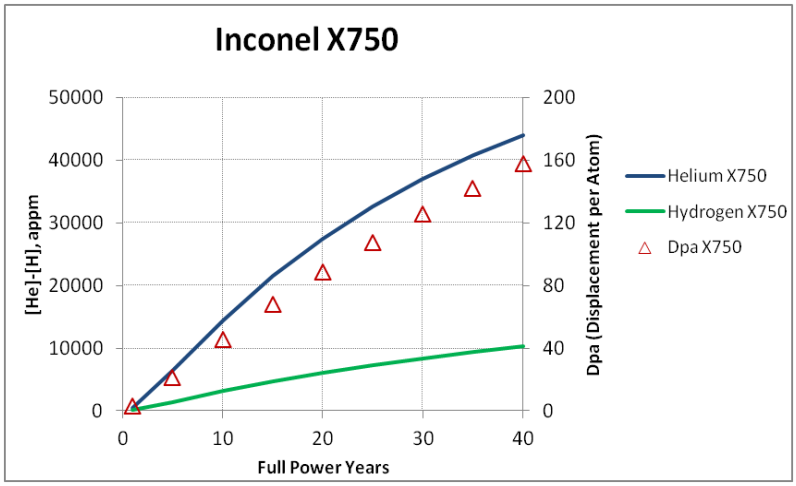

Figure 2.6: Calculated helium, hydrogen and displacement per atom for Inconel X750 (at maximum concentration of Ni) in the core of the CANDU reactor [20].

Table 2.2: Calculated data for Inconel X750 at minimum concentration of Ni [22].

DPA	HELIUM(appm)	HYDROGEN(appm)	YEAR
2.78	467.23	145.64	1
20.50	5962.74	1333.64	5
43.77	13436.43	2919.52	10
65.26	19940.05	4343.43	15
85.06	25515.43	5612.40	20
103.40	30291.40	6747.86	25
120.49	34383.21	7769.21	30
136.50	377889.88	8692.71	35
151.60	40894.90	9534.80	40

(Estimated error ≈ 5%)

Table 2.2 shows the calculated data for Inconel X750 at minimum concentration of Ni and the calculated values of H, He and DPA generation as a function of time in the CANDU reactor for Inconel X750 at minimum concentrations of Ni is shown in Figure 2.7:

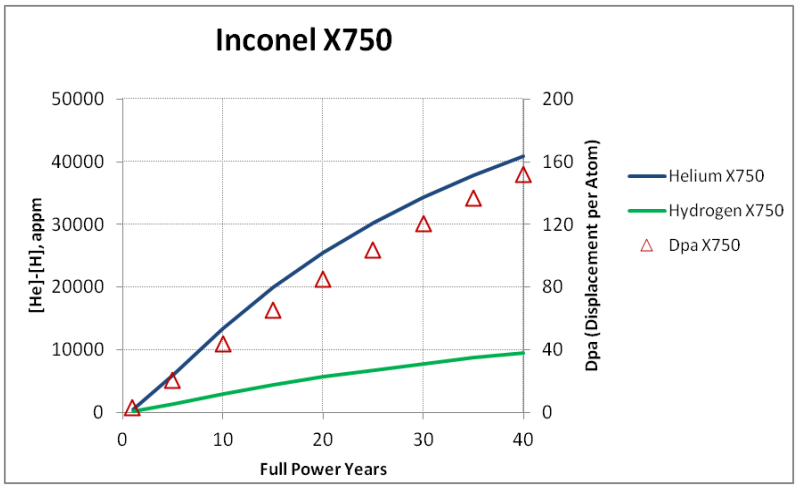

Figure 2.7: Calculated helium, hydrogen and displacement per atom for Inconel X750 (at minimum concentration of Ni) in the core of the CANDU reactor [20].

It was observed that the gas production rates and DPA (Displacement per Atom) were only slightly enhanced at maximum concentration of Ni in the Inconel X750 alloy compared to the minimum concentration.

Table 2.3 shows the calculated data for pure nickel.

Table 2.3: Calculated data for Pure Ni [22].

DPA	HELIUM(appm)	HYDROGEN(appm)	YEAR
3.18	688.93	212.12	1
25.68	8793.28	1953.49	5
55.43	19814.96	4278.98	10
82.56	29405.95	6365.60	15
107.20	37627.93	8223.70	20
129.68	44670.91	9884.90	25
150.33	50704.89	11377.80	30
169.39	55875.87	12726.40	35
187.11	60306.85	13952.10	40

(Estimated error ≈ 5%)

Figure 2.8 shows the calculated values of H, He and DPA generation as a function of time for Pure Ni.

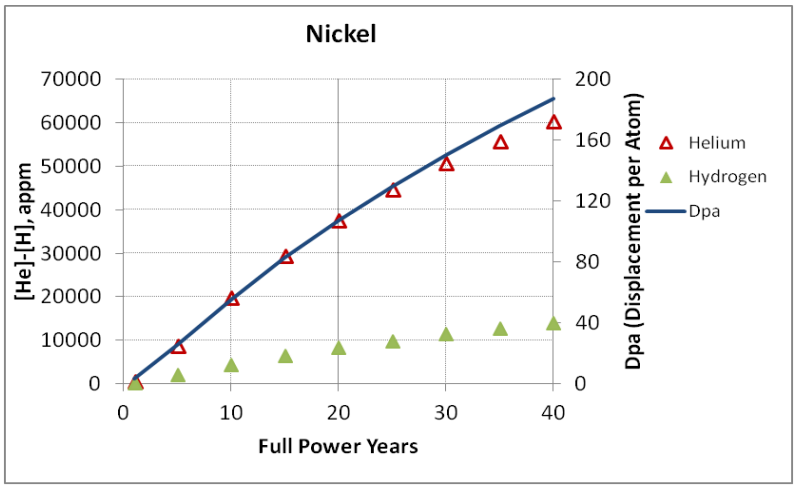

Figure 2.8: Calculated helium, hydrogen and displacement per atom for pure Ni [20].

From figure 2.8, it is observed that the gas production rates and DPA are significantly higher in pure Ni as compared to Inconel X750. It means that higher concentration of Ni in the alloy leads to higher gas production rates which would eventually cause failure at a faster rate.

To summarize, previous studies suggest that Inconel X750 spacers tend to fail over a period of time because of transmutation of ^{58}Ni to ^{59}Ni, which then leads to various other reactions producing excess helium and hydrogen. It can also be clearly seen that the helium voids are

accumulated more towards the grain boundaries rather than the bulk of the material, but there is not enough research done which relates the helium accumulation to the type of grain boundaries (low energy or high energy). The main focus of this report would be to first optimize the technique of helium ion implantation as it is not safe and cost effective to deal with ex-service spacers. This will be followed by finding out the optimum temperature to observe the helium voids which would help in establishing a relationship between the grain boundary structure and the accumulation of voids. All the experiments would be carried out for Inconel X750 and for pure Ni since many Ni based alloys are used in the nuclear industry and it would be interesting to study the effect of Helium production and degradation of properties of pure Ni. This would help to evaluate performance of Ni alloys in present and future nuclear reactors.

CHAPTER THREE

MATERIALS AND METHODOLOGY

In this chapter I discuss in detail the materials analysed and various experimental techniques that were used to achieve the desired objectives. Also in this chapter various difficulties that we faced while conducting the experiments are discussed.

3.1 Materials

The two metals viz. Pure Ni and Inconel X750 were used for analysis. Pure Ni sheets (with a thickness of 0.050″ and 99.9% purity) were ordered from ESPI Metals. Inconel X750 sheets (with a thickness of 0.050″) were ordered from Haynes International. Chemical composition (wt. %) of Inconel X750 can be seen in Table 3.1[23].

X750 is a precipitation hardened nickel based superalloy with high strengths upto 1300°F. This alloy is known for its corrosion and oxidation resistance properties [23].

Table 3.1: Chemical composition of Inconel X750 alloy (wt. %).

Element	Wt. %
Nickel (plus Cobalt)	70.00 min.
Chromium	14.0-17.0
Iron	5.0-9.0
Titanium	2.25-2.75
Aluminium	0.40-1.00
Niobium (plus Tantalum)	0.70-1.20
Manganese	1.00 max.
Silicon	0.50 max.
Sulfur	0.01 max.
Copper	0.50 max.
Carbon	0.08 max.

3.2 Methodology

In order to observe the formation of Helium bubbles on Pure Ni and Inconel X750 alloy the technique of Helium ion-implantation was adopted (as it was not possible to deal with

radioactive specimens from CANDU reactors). This was primarily on account of various health and safety concerns.

The first objective of this study was to optimize the helium ion implantation technique to obtain the appropriate amount of helium required to observe voids. A quantity of 1800appm was selected because any quantities of helium greater than this would have been difficult to implant using the implantation apparatus used and previous studies showed void formation at 1800appm [6]. In order to proceed with the helium ion implantation various simulations were done using SRIM (*The Stopping and Range of Ions in Matter*) software which helped us obtain various parameters necessary for carrying out the implantations. Details of SRIM simulation are discussed below.

3.2.1 SRIM Simulation

SRIM (The Stopping and Range of Ions in Matter) software was used to determine the implantation parameters and also for the calculation of fluence. SRIM is a combination of programs which is used to calculate the range of penetration of ions in matter using a quantum mechanical treatment of ion-atom collisions. SRIM was initially released in 1983 by its developers James F. Ziegler and Jochen P. Biersack, and is constantly updated [24].

Implantation parameters like projected range and longitudinal straggling were determined using SRIM which were then used for the calculation of fluence and concentration of implanted ions, using equations 3.1 and 3.2. Fluence is defined as the number of particles incident on a sphere of cross-sectional area.

$$Concentration\ of\ implanted\ ions = \frac{atom\% \times target\ density}{100} \quad (3.1)$$

$$Concentration\ of\ implanted\ ions\ = \frac{fluence}{2 \times longitudinal\ straggle} \quad (3.2)$$

The simulations were carried out at implantation energy of 150 keV, keeping in mind the limitations of the implantation equipment used. For each of the specimens (Pure Ni and Inconel X750) the simulations were carried out independently at an ion energy range of 150keV.

In SRIM the user provides the input information like the implanted ion type, chemical composition of the target compound and the ion energy range over which the calculation has to be performed.

Figure 3.1 shows the SRIM input window in which the user provides the information of the ion to be implanted, the target metal composition, target metal density and the range over which the implantation is to take place. Based on these inputs the software performs various calculations and provides us with the output files.

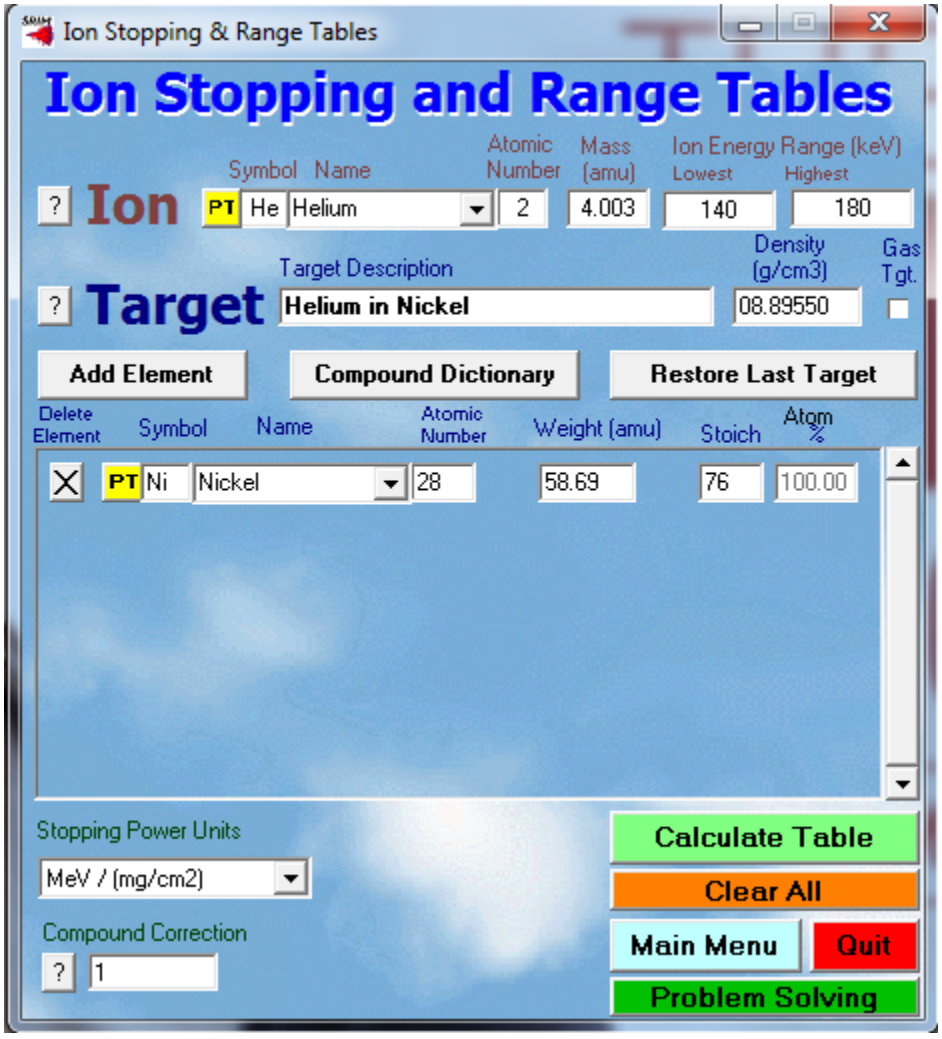

Figure 3.1: SRIM input window.

Table 3.2 and Table 3.3 shows the output files from SRIM software for Pure Ni and Inconel X750. These output files gives us the projected range and longitudinal straggling for various Ion energies which is then used to calculate the concentration of implanted ions and fluence.

Table 3.2: Output file of SRIM simulation software for Pure Nickel.

```
==================================================================
               SRIM version ---> SRIM-2013.00
               Calc. date   ---> July 24, 2015
 ==================================================================

 Disk File Name = SRIM Outputsin Nickel.txt

 Ion = Helium [2], Mass = 4.003 amu

 Target Density = 8.8955E+00 g/cm3 = 9.1274E+22 atoms/cm3
 ======= Target Composition ========
    Atom   Atom   Atomic    Mass
    Name   Numb   Percent   Percent
    ----   ----   -------   -------
     Ni     28    100.00    100.00
 ====================================
 Bragg Correction = 0.00%
 Stopping Units = MeV / (mg/cm2)
 See bottom of Table for other Stopping units

     Ion        dE/dx      dE/dx     Projected  Longitudinal   Lateral
   Energy       Elec.     Nuclear     Range     Straggling   Straggling
 -------------  ---------- ---------- ----------  ----------  -----
 140.00 keV   4.823E-01  6.466E-03    3781 A      1141 A      1160 A
 150.00 keV   4.977E-01  6.165E-03    3983 A      1162 A      1191 A
 160.00 keV   5.120E-01  5.894E-03    4180 A      1180 A      1220 A
 170.00 keV   5.254E-01  5.649E-03    4374 A      1198 A      1248 A
 180.00 keV   5.379E-01  5.426E-03    4564 A      1214 A      1274 A
------------------------------------------------------------
 Multiply Stopping by        for Stopping Units
 -------------------        ------------------
  8.8952E+01                 eV / Angstrom
  8.8952E+02                keV / micron
  8.8952E+02                MeV / mm
  1.0000E+00                keV / (ug/cm2)
  1.0000E+00                MeV / (mg/cm2)
  1.0000E+03                keV / (mg/cm2)
  9.7456E+01                 eV / (1E15 atoms/cm2)
  1.0590E+01                L.S.S. reduced units
 ==================================================================
 (C) 1984, 1989,1992,1998,2008 by J.P. Biersack and J.F. Ziegler
```

According to SRIM simulation the projected range and longitudinal straggling for Pure Nickel has been estimated to be 3983Å and 1162Å respectively. Using equations 1 and 2 the

concentration of implanted ions and fluence has been calculated to be 1.641E+21 ion/cm^3 and 3.818E+17 ion/cm^2 respectively.

Table 3.3: Output file of SRIM simulation software for Inconel X750.

```
==================================================================
              SRIM version ---> SRIM-2013.00
              Calc. date   ---> July 25, 2015
 ==================================================================

 Disk File Name = SRIM Outputsin Cr-Fe-Ni-Ti.txt

 Ion = Helium [2], Mass = 4.003 amu

 Target Density = 8.0300E+00 g/cm3 = 8.4855E+22 atoms/cm3
 ======= Target Composition ========
    Atom   Atom   Atomic    Mass
    Name   Numb   Percent   Percent
    ----   ----   -------   -------
     Cr     24    018.02    016.44
     Fe     26    007.21    007.07
     Ni     28    072.07    074.22
     Ti     22    002.70    002.27
 ====================================
 Bragg Correction = 0.00%
 Stopping Units = MeV / (mg/cm2)
 See bottom of Table for other Stopping units

    Ion        dE/dx      dE/dx     Projected  Longitudinal   Lateral
  Energy       Elec.      Nuclear     Range     Straggling   Straggling
 -------------  ---------- ---------- ----------  ----------  -------
 140.00 keV   5.231E-01  6.440E-03    3896 A      1169 A      1194 A
 150.00 keV   5.400E-01  6.139E-03    4135 A      1179 A      1214 A
 160.00 keV   5.557E-01  5.869E-03    4308 A      1206 A      1253 A
 170.00 keV   5.704E-01  5.623E-03    4507 A      1222 A      1280 A
 180.00 keV   5.841E-01  5.400E-03    4703 A      1238 A      1305 A
-------------------------------------------------------------
 Multiply Stopping by        for Stopping Units
 -------------------        ------------------
  8.0297E+01                 eV / Angstrom
  8.0297E+02                keV / micron
  8.0297E+02                MeV / mm
  1.0000E+00                keV / (ug/cm2)
  1.0000E+00                MeV / (mg/cm2)
  1.0000E+03                keV / (mg/cm2)
  9.4629E+01                 eV / (1E15 atoms/cm2)
  1.0274E+01                L.S.S. reduced units
 ==================================================================
 (C) 1984, 1989,1992,1998,2008 by J.P. Biersack and J.F. Ziegler
```

According to SRIM simulation the projected range and longitudinal straggling for Inconel X750 has been estimated to be 4135Å and 1179Å respectively. Using equations 1 and 2 the concentration of implanted ions and fluence has been calculated to be 1.562E+21 ion/cm^3 and 3.683E+17 ion/cm^2 respectively.

The following table summarizes the data obtained from SRIM and the calculations made, which were then used to carry out the Helium ion implantation.

Table 3.4: Range, Fluence and Concentration of Implanted Ions for Pure Ni and Inconel X-750.

Sample	**Projected Range(Å)**	**Longitudinal Straggling(Å)**	**Concentration of Implanted Ions (ion/cm^3)**	**Fluence (ion/cm^2)**
Inconel X750	4135	1179	1.562E+21	3.683E+17
Pure Ni	3983	1162	1.641E+21	3.818E+17

Once the above parameter was obtained, we started with the helium ion implantation.

3.2.2 Helium Ion-Implantation

Helium Ion-implantations were carried out using a Tandem accelerator at the Ion Beam Laboratory, University of Montreal. This accelerator was initially installed at the Chalk River Laboratories in 1954 and was then transferred to University of Montreal in 1966 [25]. The Tandem accelerator works on the same principle as that of a Tandetron.

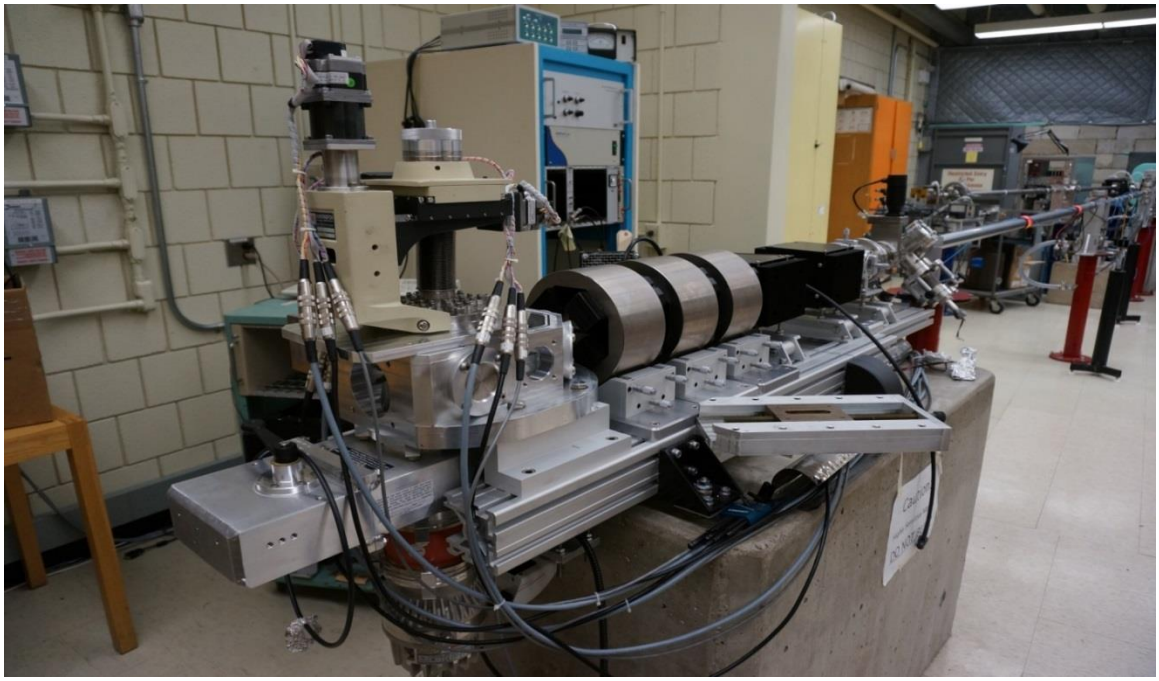

Figure 3.2: Tandetron accelerator at the University of Montreal [25].

The implantations were carried out using a beam current of 3μA and implantation energy of 150keV for a time period of 20 minutes. The energy of 150keV was selected considering the implantation limitations of the accelerator.

Ion implantation is a technique by which ions of a material are accelerated in an electric field and then impacted into another material. It is basically a high-energy surface-modification process. Ion implantation process does not introduce any dimensional change on the surface of the object being treated and is a low temperature treatment process as a result it does not cause thermal distortion of the object [26].

Once the implantation was carried out we moved to our second objective which was to establish a relationship between temperature and accumulation of voids.

3.2.3 Vacuum Annealing

The post implanted samples were vacuum annealed at 400^{o}C, 500^{o}C, 600^{o}C and 700^{o}C before carrying out microstructural evaluation. They were annealed in vacuum in order to avoid oxidation. The main purpose behind annealing was to understand the relationship between temperature and the production of Helium voids and to initiate the Helium diffusion, as previous studies have suggested that Helium voids are formed at higher temperatures thus annealing was

done to increase the diffusion rate of Helium, which would help us to observe the Helium bubbles at higher temperatures.

The initial plan was to vacuum anneal the samples in a vacuum furnace but due to non-availability of a vacuum furnace the samples were vacuum sealed in glass tubes and then heated in a Thermo Scientific Thermolyne™ furnace.

Figure 3.2 shows the various Pure Ni samples which have been vacuum sealed prior to annealing at various temperatures.

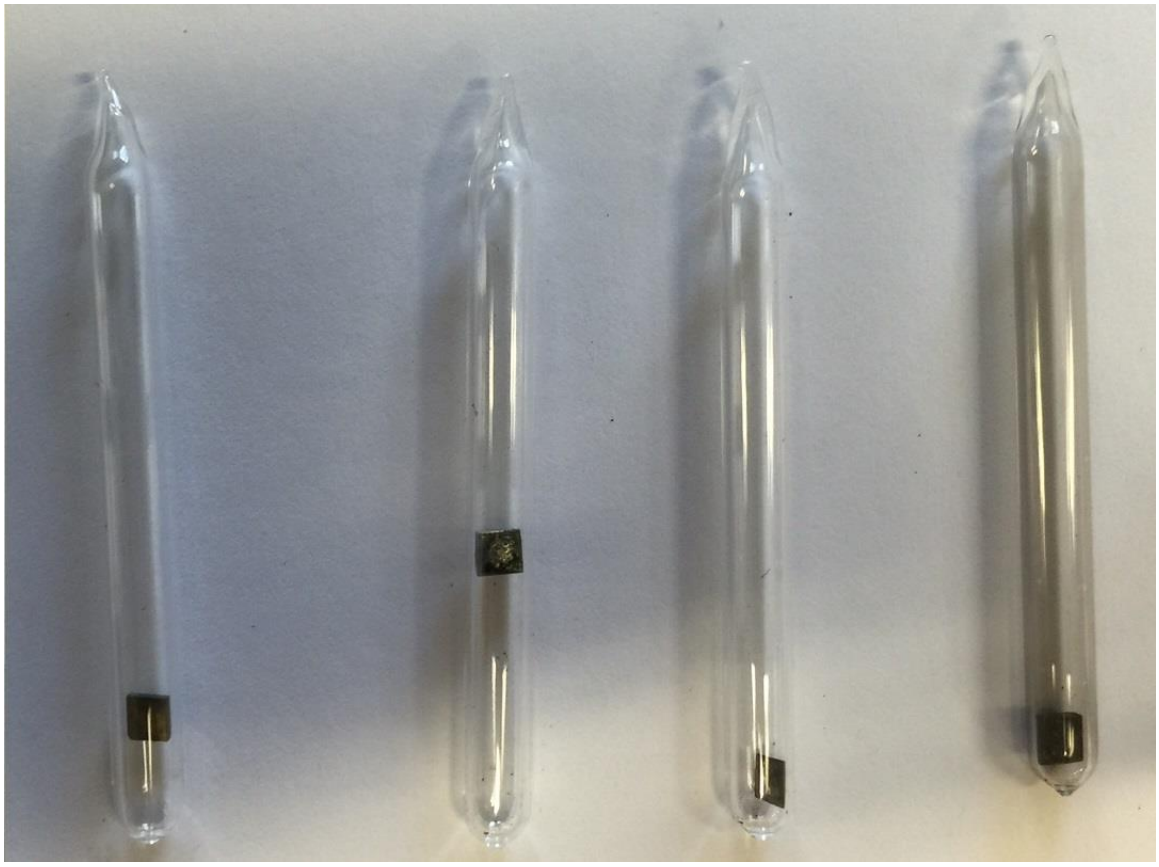

Figure 3.3: Samples vacuum sealed in glass tubes.

3.2.4 Microstructural Evaluation

Microstructural evaluation of the specimens before and after implantation was preceded by metallographic sample preparation, which began with hot-mounting of specimens using PolyFast, a black bakelite hot mounting resin with carbon filter in a SimpliMet™ XPS1

Mounting System. This was followed by grinding and polishing (diamond and vibratory) of the specimens to obtain a mirror like finish surface. For the purpose of grinding, 180, 220, 320, 500, 800, 1200, 2000 and 4000 grade SiC grinding foils were used. Diamond polishing was done using 3 µm MD-Mol with 3 µm MD-Mol suspension and 1 µm MD-Nap clothes with 1 µm MD-Nap suspension. The final stage of polishing was the chemo-mechanical polishing using the VibroMet®2 vibratory polisher using MasterMet 2 collidal silica solution (in order to obtain a stress-free surface).

3.2.5 Scanning Electron Microscopy (SEM) and Electron Backscattered Diffractometry (EBSD)

SEM and EBSD measurements were performed on implanted, non-implanted, annealed and non-annealed samples using a SU 6000 Hitachi field emission scanning electron microscope. AZTEC 2.0 data acquisition software was used to acquire the electron diffraction patterns. The raw EBSD data was analysed using Oxford Instruments Channel 5 processing software. This software was used to define the grains orientation, grain boundary misorientation and to obtain the grain size diameter.

SEM measurements were done on implanted samples annealed to different temperatures (400^{o}C, 500^{o}C, 600^{o}C and 700^{o}C) in order to establish a relationship between temperature and accumulation of helium voids. Both the alloys were first annealed to different temperatures and were then observed using the SEM. SEM scans were made at these temperatures and the required relationship was established.

Once the relationship between the temperature and accumulation of voids was established, investigations were initiated towards achieving the last objective of the study viz., to study the influence of grain boundary structure on the accumulation of voids. In order to achieve this objective, the same annealed samples were used for EBSD analysis but unfortunately no results could be obtained. This could be because the samples had oxidized over a period of time due to improper storage and constant annealing at different temperatures. The annealing was done in vacuum sealed glass tubes but it is believed that vacuum was not sufficiently good. Due to this slight oxidation of the samples, the grains were not indexed and thus no diffraction pattern was

obtained using EBSD. As a result fresh samples had to be made and a marking technique was developed in order to mark the samples. The samples were marked prior to implantation followed by EBSD scans over that marked area in order to get the grain map for the non-implanted samples. The implantation was then carried out on these samples. Once the implantation was carried out the samples were then vacuum annealed followed by SEM scans over the marked area. After implantation and annealing SEM scans were done and not EBSD scans because of a slight oxidation layer that prevented obtaining an EBSD pattern after annealing.

The SEM scans done after implantation and annealing were then compared to the EBSD scans obtained prior to implantation. This helped to achieve the relationship between the grain boundary structure and the accumulation of voids.

Micro-hardness marking technique was used in order to observe the same area before and after implantation. Marks on the sample were made using a Mitutoyo MVK-H1 Micro-hardness Tester. Figure 3.3 shows the mirco-hardness marking done on pure Ni sample.

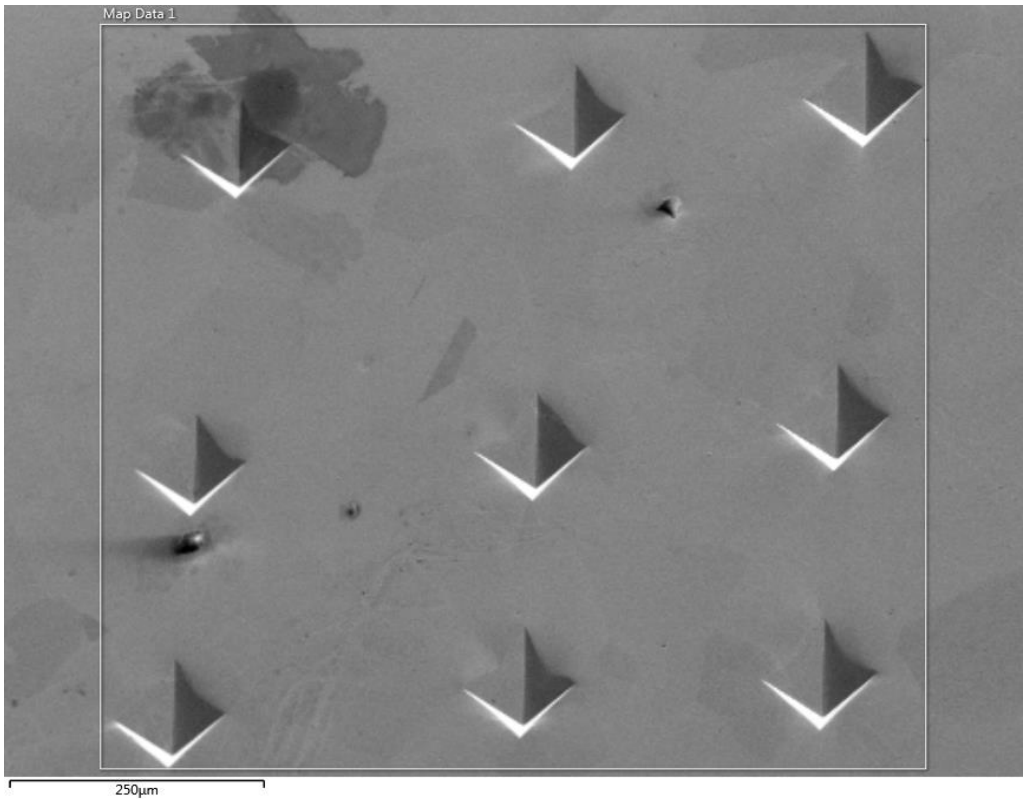

Figure 3.4: Micro-hardness marking on pure Ni sample.

3.2.6 Transmission Electron Microscopy (TEM)

TEM studies of the implanted annealed samples were done at CanmetMATERIALS, Hamilton, Ontario. CanmetMATERIALS is one of the largest research centers in Canada which is dedicated to fabricating, processing and evaluating metals and materials [27].

TEM samples were prepared using the FIB (Focused Ion Beam) lift-out technique. TEM study was carried out using FEI's Tecnai Osiris TEM equipped with X-FEG gun at 200kV and EDS (Energy Dispersive Spectroscopy) mapping was done using ESPRIT software.

TEM imaging was done for pure Ni sample which was implanted and vacuum annealed at 700^{o}C. TEM imaging was also done at the oxide layer formed due to vacuum annealing of the InconelX750 sample. TEM imaging of the oxide layer was done to understand more about the oxide formed that created problems performing the EBSD experiments.

CHAPTER FOUR

RESULTS AND DISCUSSION

This chapter discusses the results and is divided into two sections. The first section discusses in details the relationship between annealing temperature and helium void formation and the relationship established between helium voids accumulation and grain boundary misorientation for Pure Ni. The second section discusses the relationships established for Inconel X750 alloy.

4.1 Pure Nickel

Microstructural analysis was performed on pure Ni before and after implantation. SEM scans were done to establish a relationship between helium void formation and annealing temperatures while EBSD imaging was done to establish a relationship between helium void concentration and grain boundary misorientation. TEM imaging was also performed on implanted vacuum annealed pure Ni samples which acted as confirmatory tests for helium void formation.

4.1.1 Relationship between helium voids and annealing temperatures for Pure Ni

SEM scans were done on pure Ni samples after implantation. After implantation the samples were vacuum annealed at different temperatures in order to increase the diffusion of the helium atoms. SEM scans were done at all the annealed temperatures to establish a relationship between annealing temperatures and helium void formation.

The images below are the SEM images of vacuum annealed implanted Pure Ni at various temperatures.

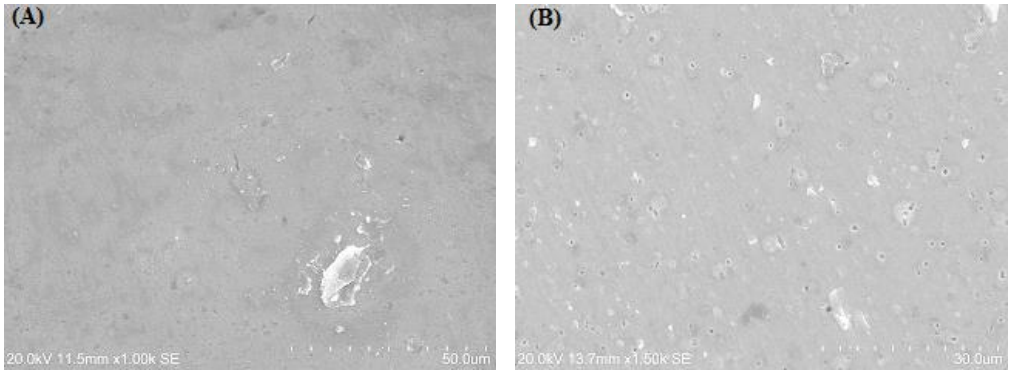

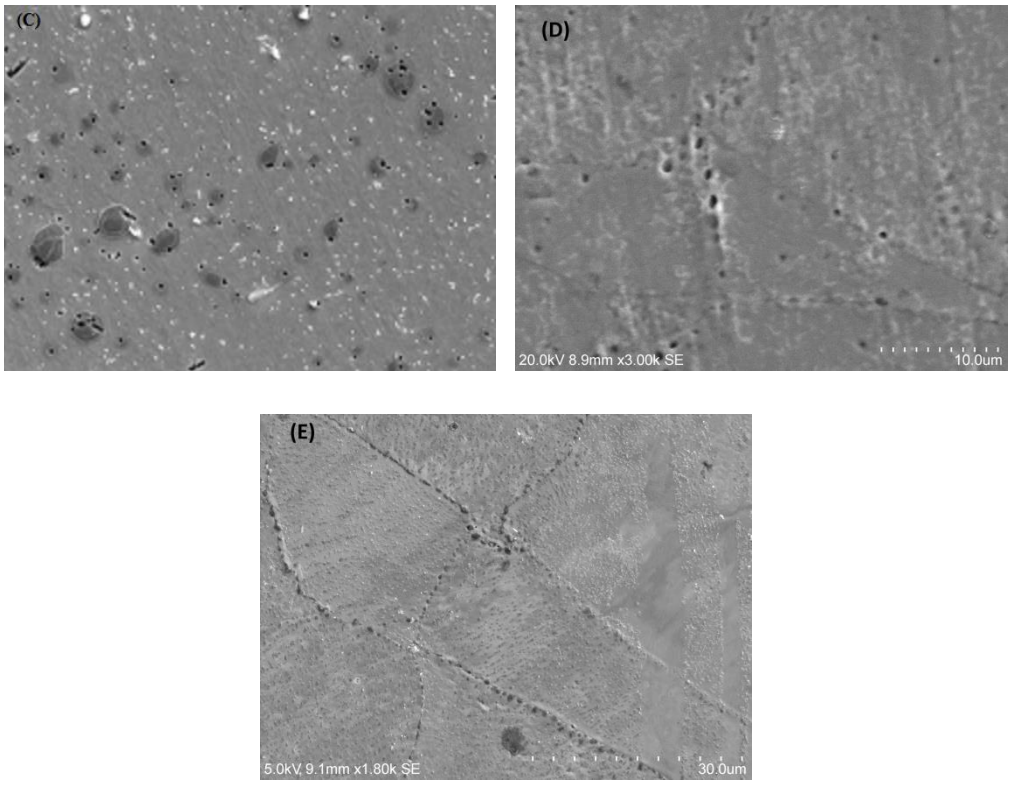

(A) As-received sample;
(B) Vacuum annealed at 400 ^{o}C;
(C) Vacuum annealed at 500 ^{o}C;
(D) Vacuum annealed at 600 ^{o}C.
(E) Vacuum annealed at 700 ^{o}C.

Figure 4.1: SEM scans of Pure Ni.

Figure 4.1 shows the SEM scans that were done at various annealed temperatures on the pure Ni sample. From the above images it could be clearly seen that no voids are observed on the as received implanted samples A, whereas voids are observed on the samples which have been vacuum annealed to 400^{o}C, 500^{o}C and 600^{o}C i.e., image B, C and D respectively. In image E which is a scan of pure Ni implanted and vacuum annealed to 700^{o}C, it can be clearly observed that the helium voids are accumulated towards the grain boundary of the sample and very few helium voids can be found in the matrix.

4.1.2 TEM scans of Pure Ni

TEM imaging of implanted Pure Ni samples were carried out. These samples had been vacuum annealed to 700^{o}C. TEM scans were done to confirm the presence of voids around the grain

boundaries. Figure 4.2 shows the various images obtained from TEM imaging of the implanted and vacuum annealed pure Ni samples.

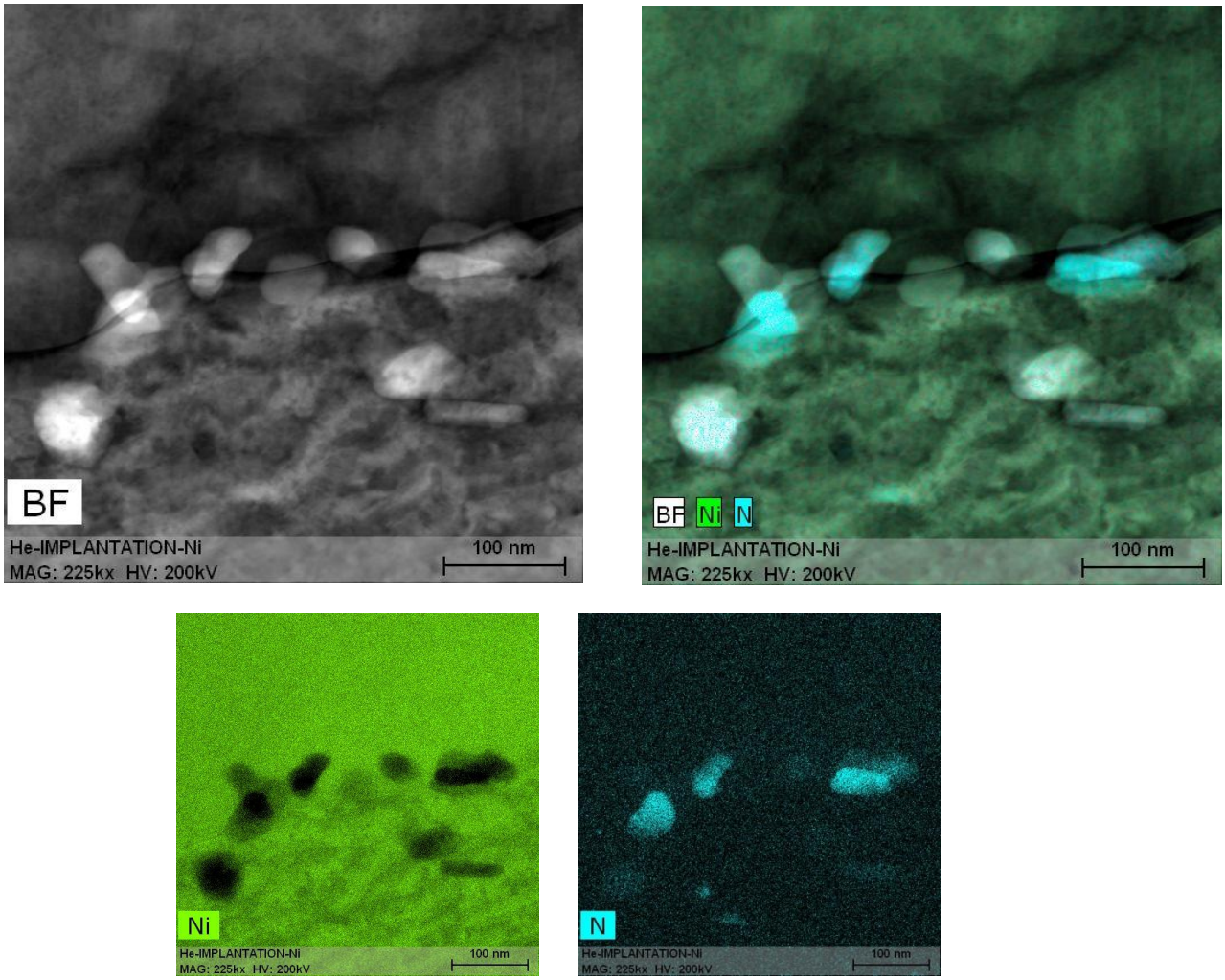

Figure 4.2: TEM scans of Pure Ni.

From the above scans it could be clearly seen that the voids are concentrated towards the grain boundaries of the material rather than the matrix or the bulk of the material. This confirms our earlier results obtained from SEM imaging of the pure Ni samples. EDS mapping was also done on the same area. From the results obtained (Figure 4.2) we can observe that the voids are having a high concentration of nitrogen. There is a high concentration of nitrogen in the voids because once the samples are annealed the trapped helium escapes creating a cavity which gets filled with air. As a result EDS imaging shows high traces of Ni where voids are formed, thus indirectly confirming the presence of helium voids at the grain boundaries rather than in the bulk of the

material. It should be noted hydrogen and helium cannot be detected using EDS technique. As a result, the EDS imaging shows concentration of nitrogen on the voids and not helium.

4.1.3 Relationship between concentration of helium voids and grain boundary misorientation for pure Ni

Once the relationship between formation of helium voids and annealing temperature was established, our final objective was to establish a relationship between concentration of helium voids and grain boundary misorientation. EBSD technique was used to measure misorientation. The samples were first marked using micro-hardness technique and then EBSD scans were taken over the marked region. Figure 4.3 shows the EBSD map of pure Ni sample prior to Helium ion implantation.

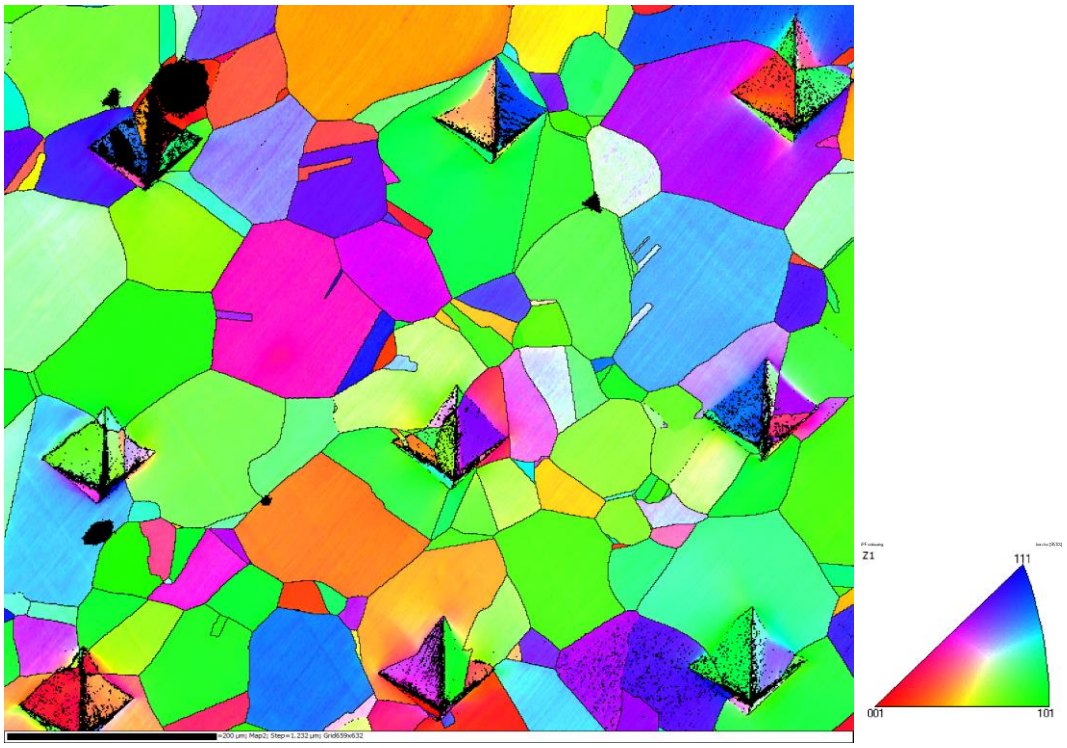

Figure 4.3: EBSD scan of pre-implanted marked Ni.

Once this EBSD scan was obtained, the samples were implanted with helium ions and were then vacuum annealed to 700^{o}C. This was done as we had previously found that at 700^{o}C, helium voids are accumulated at the grain boundary of the material. After implantation and vacuum annealing, we tried to do EBSD scans on the same area. No diffraction pattern was obtained due

to the slight oxidation layer that was formed on the sample. Consequently, we recorded SEM scans over this marked implanted vacuum annealed region to establish a relationship between helium voids accumulation and grain boundary misorientation.

The data collected from figure 4.3 was used to obtain the misorientation angle of the grain boundaries using the Oxford Instruments Channel 5 processing software. It was then used to evaluate the relationship between helium void accumulation and grain boundary misorientation.

The EBSD map below (Figure4.4) shows the pre-implanted marked area of Pure Ni. The ten small white boxes correspond to the ten different areas which were scanned using SEM after implantation and vacuum annealing of the sample at 700^{o}C. These areas are studied individually for establishing a relationship between the concentration of voids and the misorientation angle.

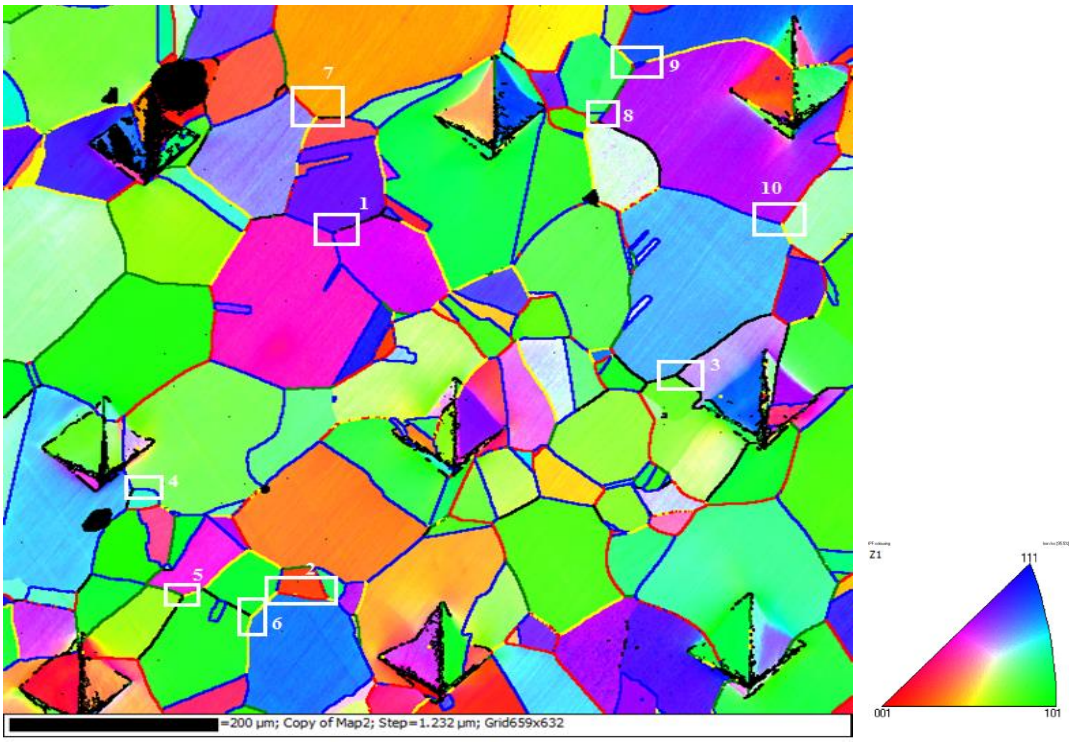

Figure 4.4: EBSD scan of pre-implanted marked Pure Ni showing the areas used for establishing the relationship between the concentration of voids and misorientation angle.

As discussed above SEM scans were carried out after implanting and vacuum annealing the samples. Below are the various SEM images that were taken at the ten different areas marked

above. The lines and numbers in these SEM images have been used to refer to the different grain boundaries.

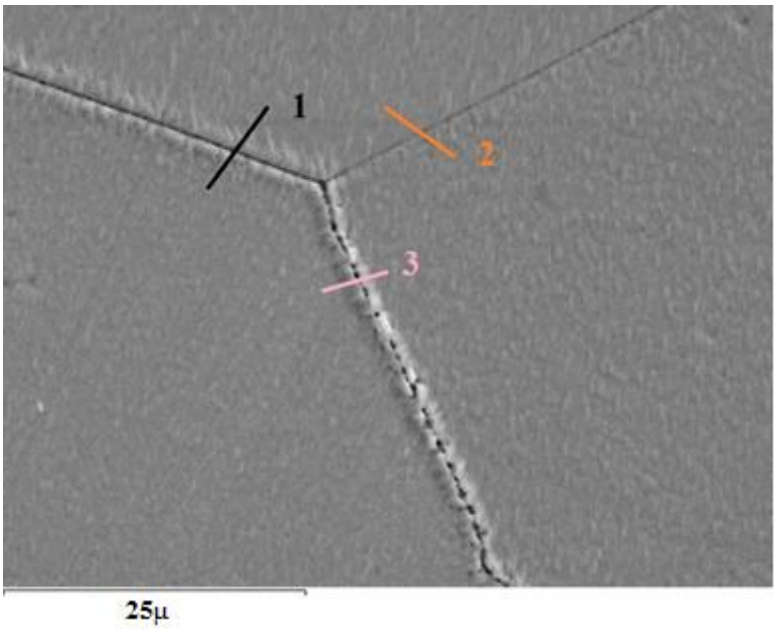

Misorientation angle for Grain Boundary 1: 61.65°
Misorientation angle for Grain Boundary 2: 9.5°
Misorientation angle for Grain Boundary 3: 55.39°

Figure 4.5: SEM Scan of Area 1.

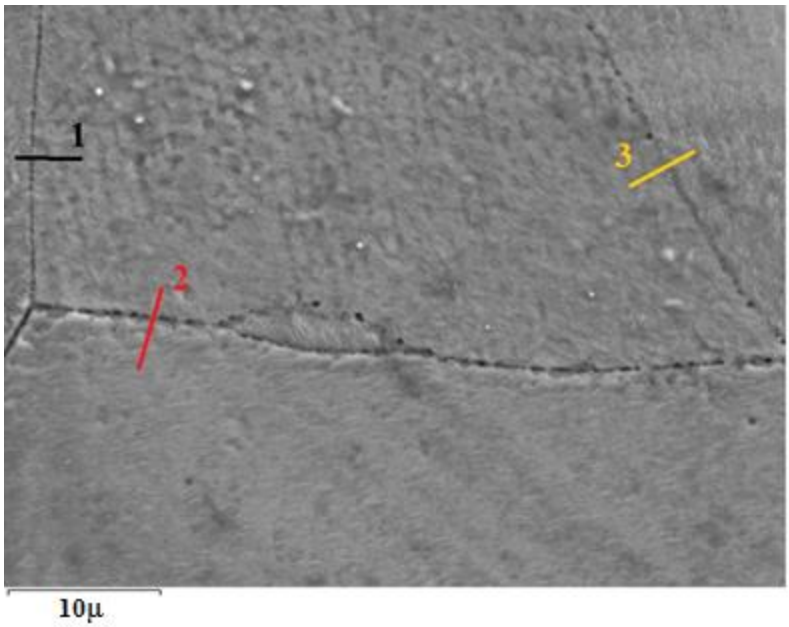

Misorientation angle for Grain Boundary 1: 56°
Misorientation angle for Grain Boundary 2: 45°
Misorientation angle for Grain Boundary 3: 48°

Figure 4.6: SEM Scan of Area 2.

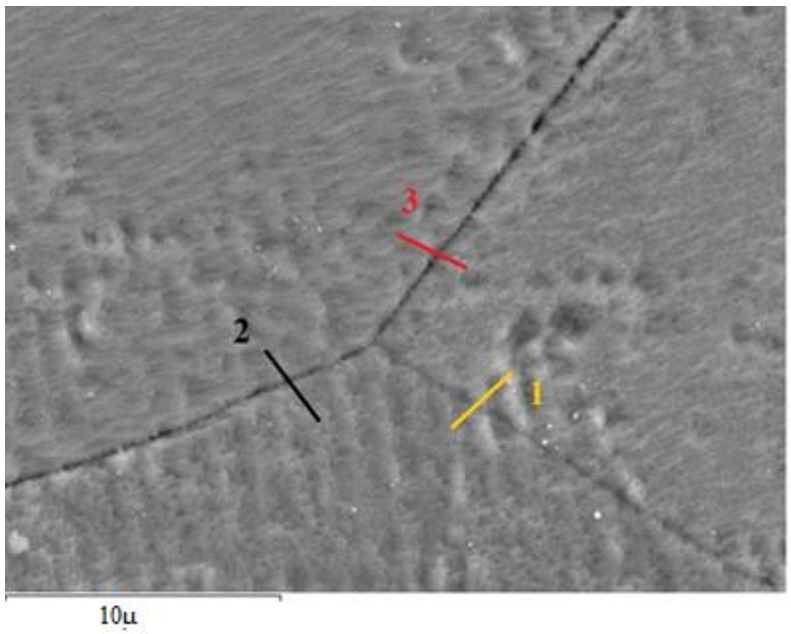

Misorientation angle for Grain Boundary 1: 13°
Misorientation angle for Grain Boundary 2: 16°
Misorientation angle for Grain Boundary 3: 12.5°

Figure 4.7: SEM Scan of Area 3.

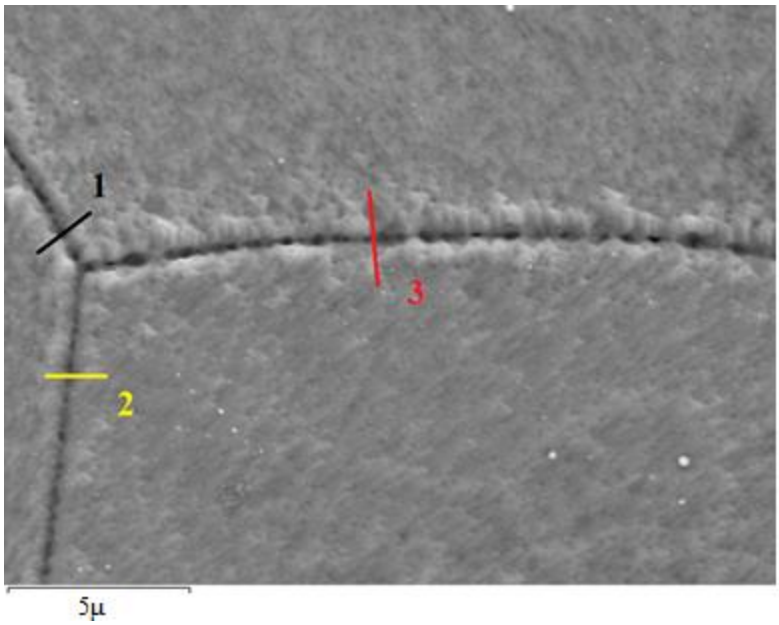

Misorientation angle for Grain Boundary 1: 56°
Misorientation angle for Grain Boundary 2: 12.56°
Misorientation angle for Grain Boundary 3: 56°

Figure 4.8: SEM Scan of Area 4.

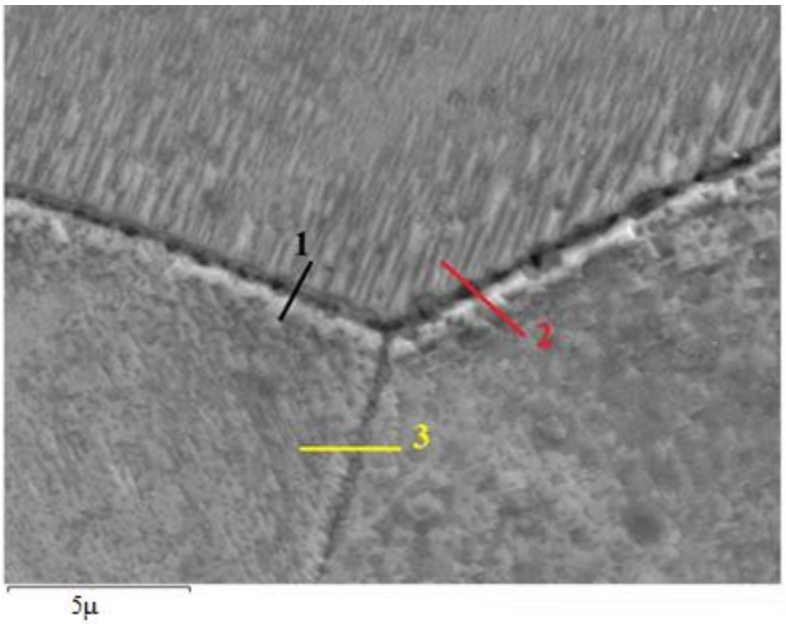

Misorientation angle for Grain Boundary 1: 23.2°
Misorientation angle for Grain Boundary 2: 32.4°
Misorientation angle for Grain Boundary 3: 12.3°

Figure 4.9: SEM Scan of Area 5.

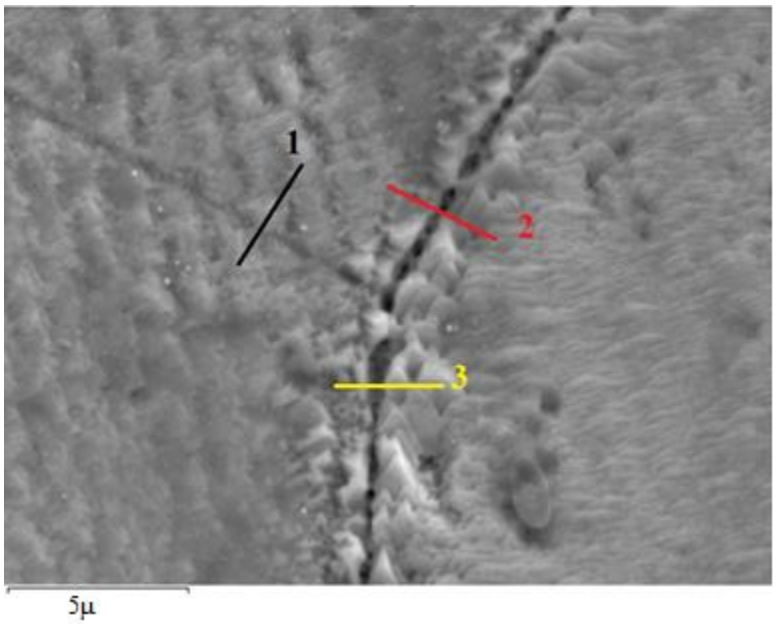

Misorientation angle for Grain Boundary 1: 11.26°
Misorientation angle for Grain Boundary 2: 38.56°
Misorientation angle for Grain Boundary 3: 33.2°

Figure 4.10: SEM Scan of Area 6.

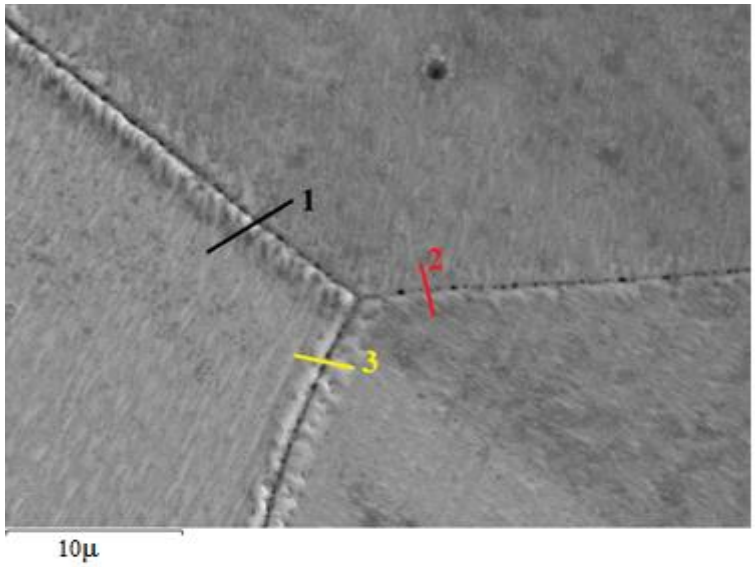

Misorientation angle for Grain Boundary 1: 46.5°
Misorientation angle for Grain Boundary 2: 20.32°
Misorientation angle for Grain Boundary 3: 35.68°

Figure 4.11: SEM Scan of Area 7.

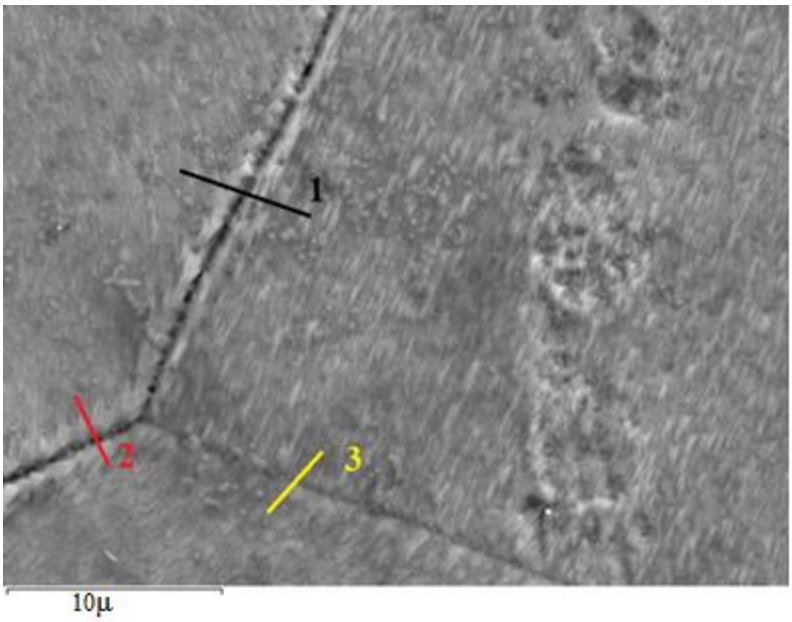

Misorientation angle for Grain Boundary 1: 22.55°
Misorientation angle for Grain Boundary 2: 50.36°
Misorientation angle for Grain Boundary 3: 14.26°

Figure 4.12: SEM Scan of Area 8.

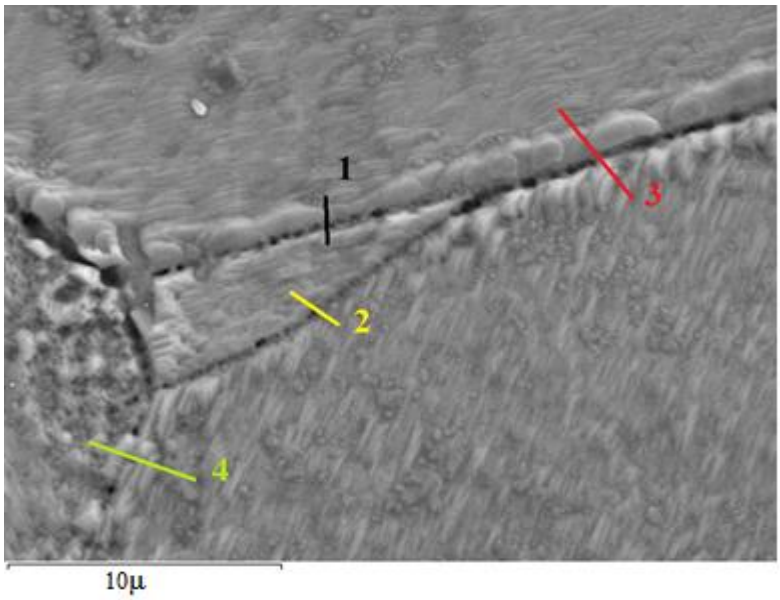

Misorientation angle for Grain Boundary 1: 50.5°
Misorientation angle for Grain Boundary 2: 52.2°
Misorientation angle for Grain Boundary 3: 32.5°
Misorientation angle for Grain Boundary 4: 22.36°

Figure 4.13: SEM Scan of Area 9.

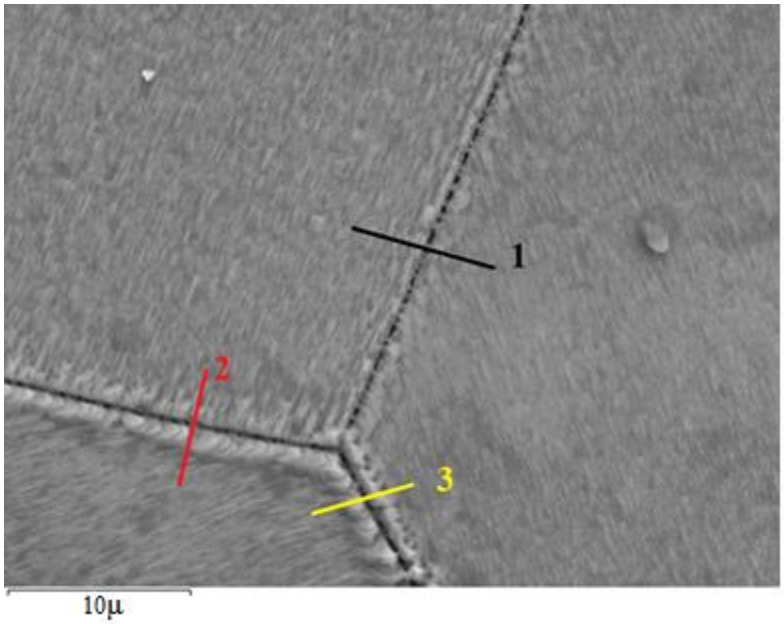

Misorientation angle for Grain Boundary 1: 47.63°
Misorientation angle for Grain Boundary 2: 52.3°
Misorientation angle for Grain Boundary 3: 33.25°

Figure 4.14: SEM Scan of Area 10.

Similarly, the entire implanted area was observed under SEM and the length of each grain boundary and number of voids on each grain boundary were calculated. Figure 4.15 shows the misorientation profile of Pure Ni sample. This figure was used to establish the relationship between the concentration of voids per micron and the misorientation angle.

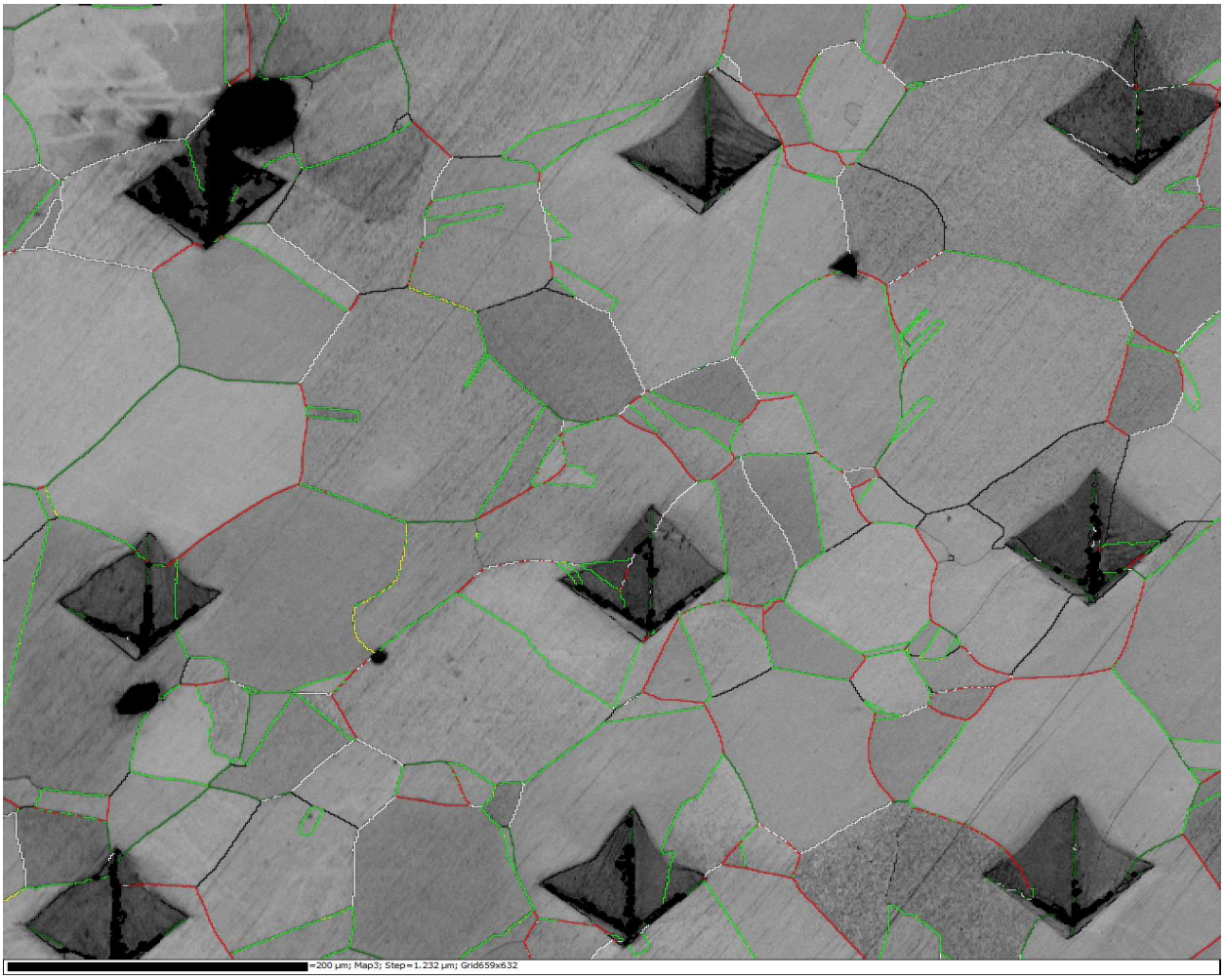

Misorientation Angle	Grain Boundary Color
>10	
>20	
>30	
>40	
>50	
>60	

Figure 4.15: The Misorientation angles for all the grain boundaries of Pure Ni.

In order to obtain the relationship between helium void accumulation and grain boundary misorientation, we first calculated the length of the grain boundaries in microns and the number

of voids corresponding to each grain boundary using SEM imaging. The data from figure 4.3 and figure 4.15 was then used to obtain the misorientation angle of the corresponding grain boundaries using the Oxford Instruments Channel 5 processing software. Once we obtained this information, the total number of voids in that grain boundary range (for example 10° - 20°) were divided by the total length of the corresponding grain boundaries in that range in order to obtain the concentration of voids per micron.

$$Concentration\ of\ voids\ per\ micron = \frac{Total\ number\ of\ voids\ corresponding\ to\ a\ grain\ boundary}{Total\ length\ of\ the\ corrersponding\ grain\ boundary} \quad (4.1)$$

Table 4.1: Concentration of voids per micron calculation for misorientation angle range 10° - 20° for pure Ni.

Grain Boundary Misorientation(degree)	No. of Voids	Length of the Grain Boundary (micron)
10.36	6	12.63
10.44	28	49.63
10.57	10	9.55
11.56	12	60.17
12.05	4	25.69
12.14	0	32.9
12.36	21	10.36
12.77	30	79.69
12.85	0	5.69
12.98	13	18.36
13.73	20	24.4
14.79	2	0.27
15.65	20	20.36
15.8	12	10.32
18.34	40	28.69
18.64	10	8.22
19.42	20	37.69
19.65	20	30.32
20	42	30.7
Total	**310**	**495.64**
Concentration of voids per micron = 310/495.64 = 0.62545		

Table 4.1 shows the calculation of concentration of voids per micron for the misorientation angle range 10° - 20° for pure Ni, similarly calculations were performed for grain boundaries range 0°-10°, 20°-30°, 30°-40°, 40°-50°, 50°-60° and 60°-70°. Table 4.2 and figure 4.16 summarizes these

calculations. In table 4.2 it could be seen that the concentration of voids per micron increases from 0.63 ± 0.16 for a misorientation angle range 0°-10° to 1.19 ± 0.16 for a misorientation angle range 60°-70°.

Table 4.2: Calculated concentration of voids per micron for pure Ni.

Misorientation angle range	Concentration of voids per micron
0°-10°	0 ± 0.16
10°-20°	0.63 ± 0.16
20°-30°	0.94 ± 0.16
30°-40°	1.07 ± 0.16
40°-50°	1.11 ± 0.16
50°-60°	1.12 ± 0.16
60°-70°	1.19 ± 0.16

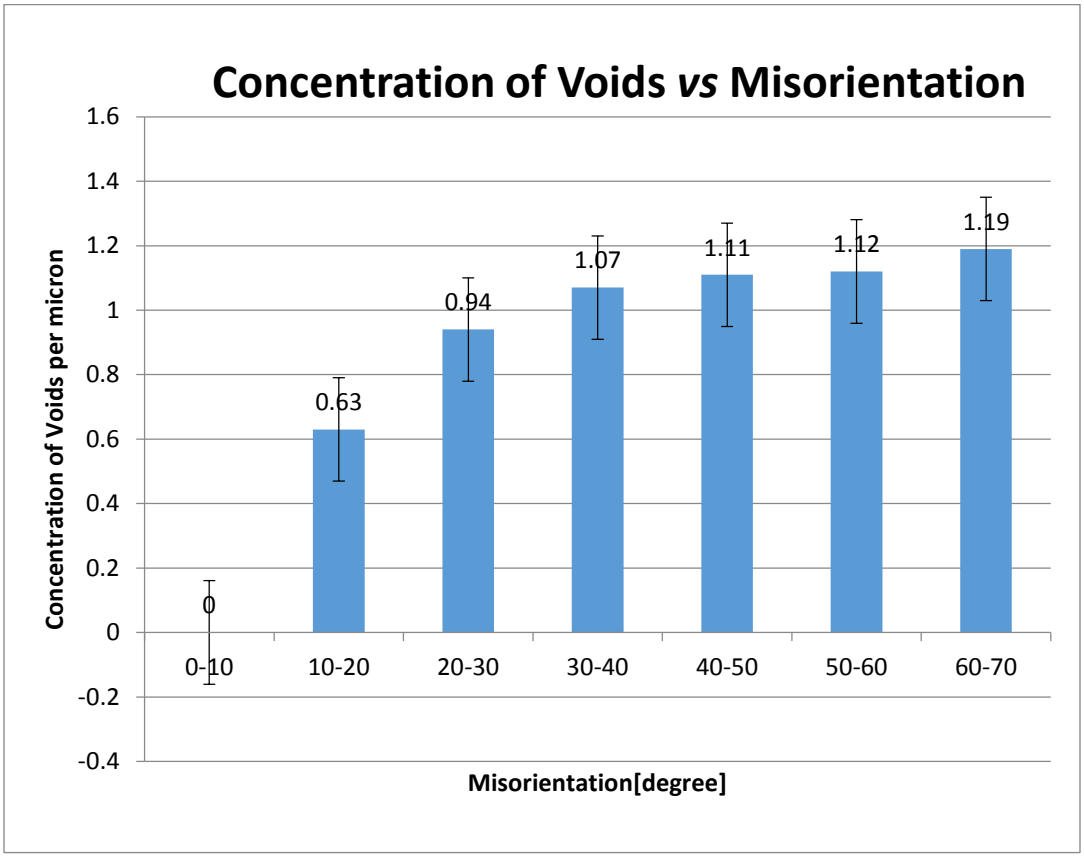

Figure 4.16: Concentration of voids per micron vs Misorientation angle for pure Ni.

It can be clearly observed from figure 4.16 that the concentration of voids per micron is increasing with an increase in the misorientation angle. This is because the energy of grain boundary increases with an increase in the misorientation angle, thus giving more free volume to the voids to form and accumulate. In can be clearly seen from figure 4.17 that the grain boundary energy is proportional to the volume expansion for pure Ni thereby meaning that at a higher energy grain boundary there would be more free volume and hence more space would be available for the helium voids to accumulate. As a result a high angle grain boundary would accumulate more voids as compared to a low angle grain boundary.

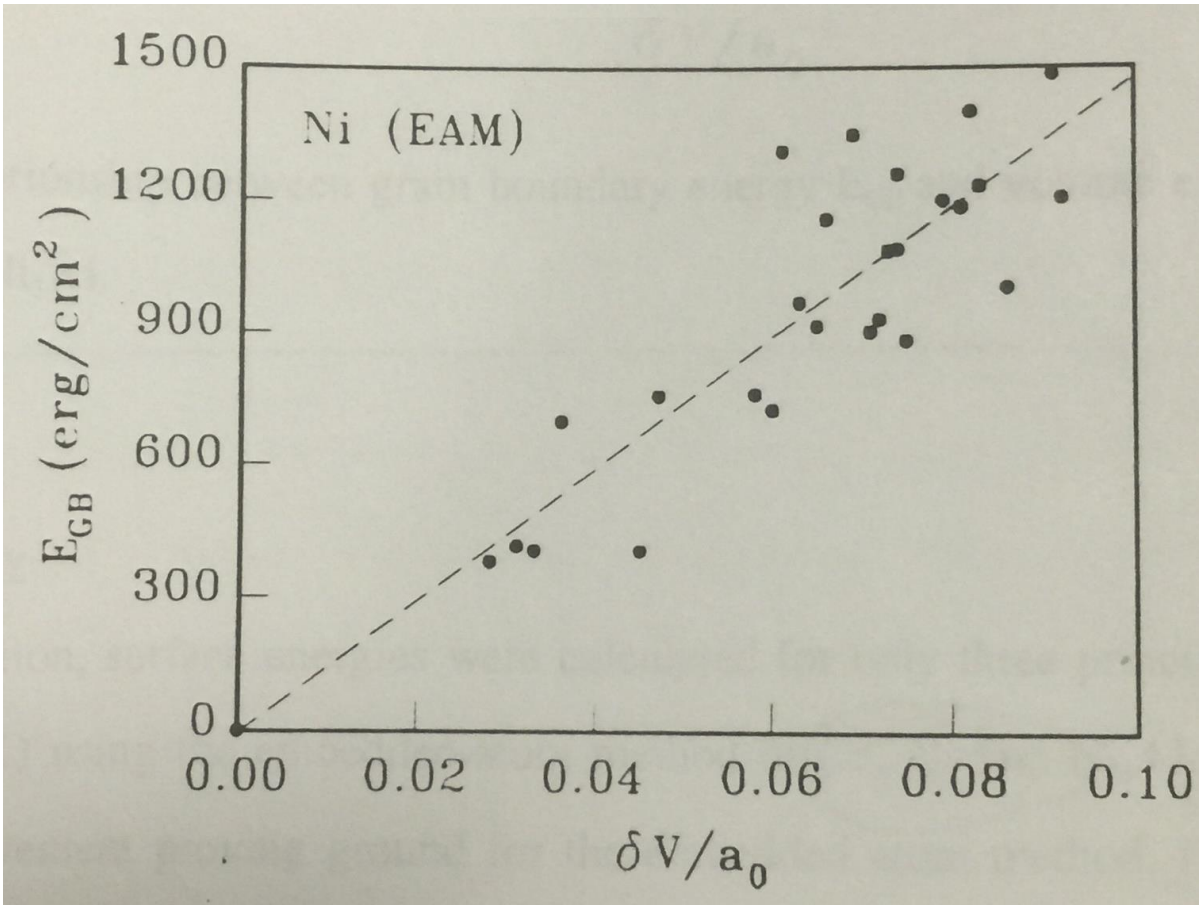

Figure 4.17: Relationship between grain boundary energy E_{GB} and volume expansion $\delta V/a_o$ for Ni [31].

Figure 4.17 was obtained using Embedded-Atom Method (EAM) Molecular Dynamics (MD) simulations done by Jian Lu as a work for his Doctor of Philosophy degree at McGill University under the supervision of Dr. J. Szpunar [31].

4.2 Inconel X750

Microstructural analysis were performed on Inconel X750 samples before and after implantation. SEM scans were done to establish a relationship between helium void formation and annealing temperatures while EBSD imaging was done to establish a relationship between helium void accumulation and grain boundary misorientation. TEM imaging was also performed on implanted vacuum annealed Inconel X750 samples to better understand the oxide layer formed during vacuum annealing which prevented us from obtaining good EBSD patterns.

4.2.1 Relationship between Helium voids and annealing temperatures for Inconel X750 alloy

SEM scans were done on Inconel X750 samples after implantation. After implantation the samples were vacuum annealed at different temperatures (400^{o}C, 500^{o}C, 600^{o}C and 700^{o}C) in order to increase the diffusion of the helium atoms. SEM scans were done at all the annealed temperatures to establish a relationship between annealing temperatures and helium void formation.

The images below are the SEM images of vacuum annealed implanted Inconel X750 at various temperatures.

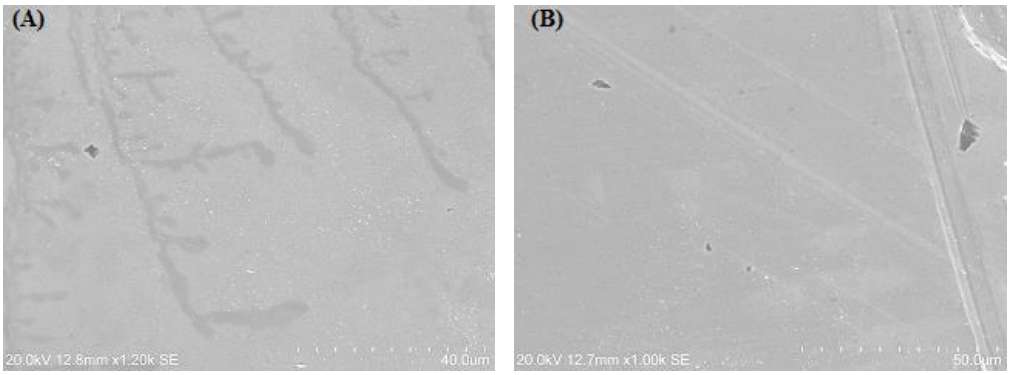

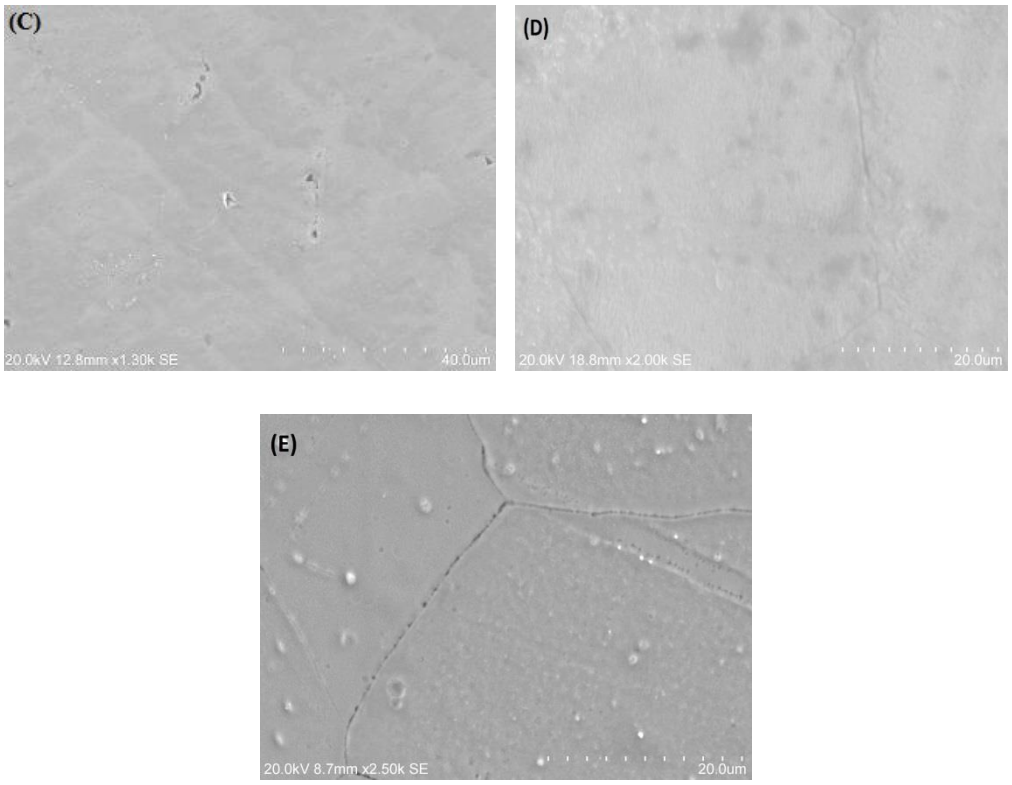

(A) As-received sample;
(B) Vacuum annealed at 400 ^{o}C;
(C) Vacuum annealed at 500 ^{o}C;
(D) Vacuum annealed at 600 ^{o}C.
(E) Vacuum annealed at 700 ^{o}C.

Figure 4.18: SEM scans of Inconel X750.

It can be clearly seen that no cavities are observed in the as received implanted samples or in the samples which have been vacuum annealed to 400^{o}C, 500^{o}C and 600^{o}C. On the other hand clear cavities can be seen in the samples which have been vacuum annealed at 700^{o}C. It can also be observed that after vacuum annealing to 700^{o}C the cavities are accumulated in proximity of grain boundaries rather than in the bulk of the material. These results obtained for Inconel X750 are similar to those obtained from pure Ni analysis and are even comparable to the experiments performed by M. Griffiths at the Canadian Nuclear Laboratories.

4.2.2 TEM scans of oxide layer formed on Inconel X750

As discussed earlier, it was difficult to perform EBSD imaging after vacuum annealing of the samples due to formation of oxide layer which prevented from obtaining EBSD diffraction pattern. As a result TEM mapping of the oxide layer was done to better understand the oxides

formed. Figure 4.19 shows the various EDS mapping images obtained from the FEI's Tecnai Osiris TEM with X-FEG gun at 200keV.

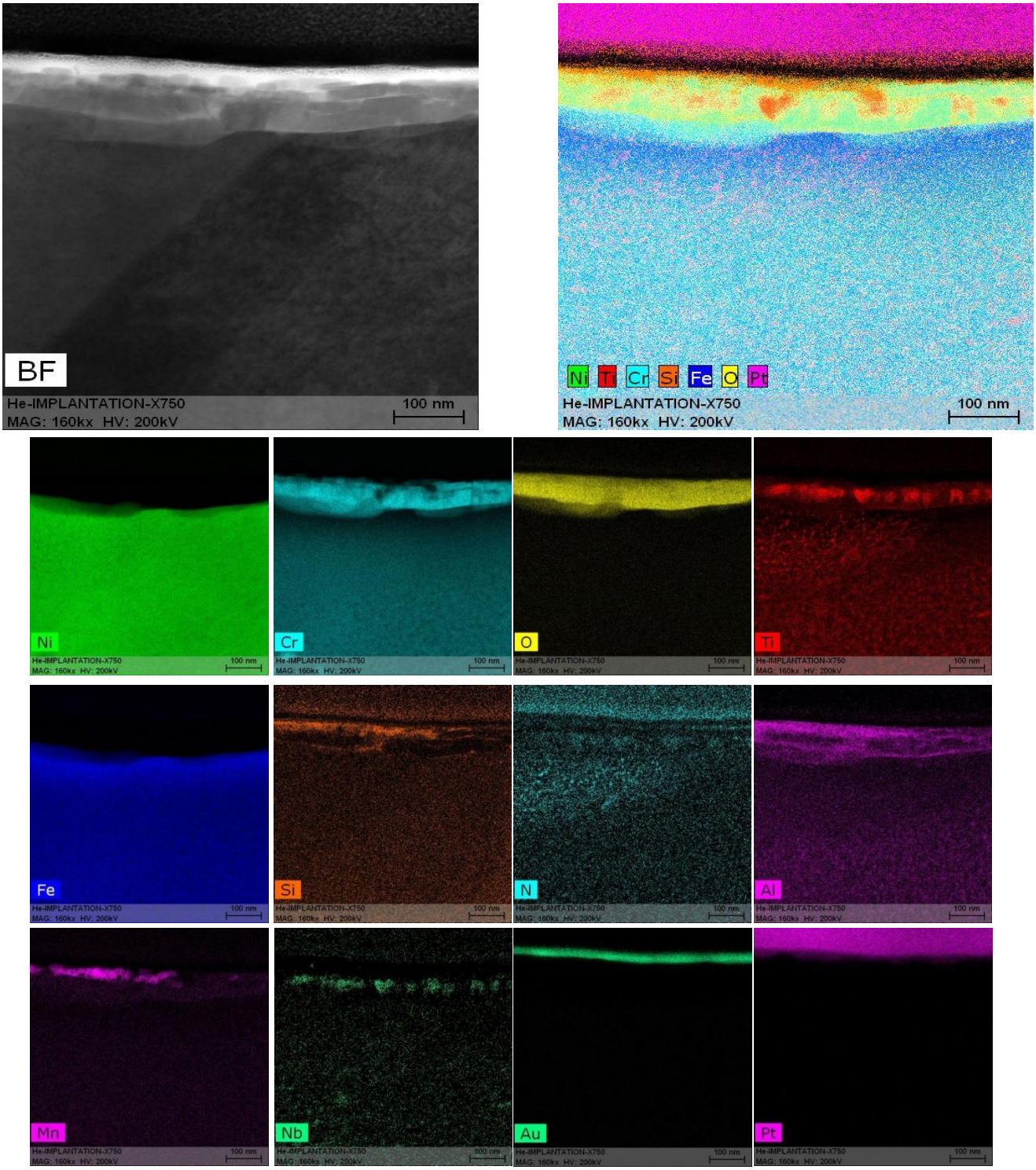

Figure 4.19: EDS scans of Inconel X750.

From the scans in figure 4.19 it was confirmed that it was the oxide layer which prevented us from obtaining an EBSD diffraction pattern. EDS analysis also showed that the oxide layer consists of oxides of chromium and titanium. Both of these metals are present in the Inconel X750 alloy.

4.2.3 Relationship between concentration of helium voids and grain boundary misorientation for Inconel X750 alloy

Once the relationship between formation of helium voids and annealing temperature was established, our objective was to establish a relationship between concentration of helium voids and grain boundary misorientation. EBSD technique was used to measure misorientation. The samples were first marked using micro-hardness technique. Thereafter, the EBSD scans were taken over the marked region. Figure 4.19 shows the EBSD map of Inconel X750 sample prior to Helium ion implantation.

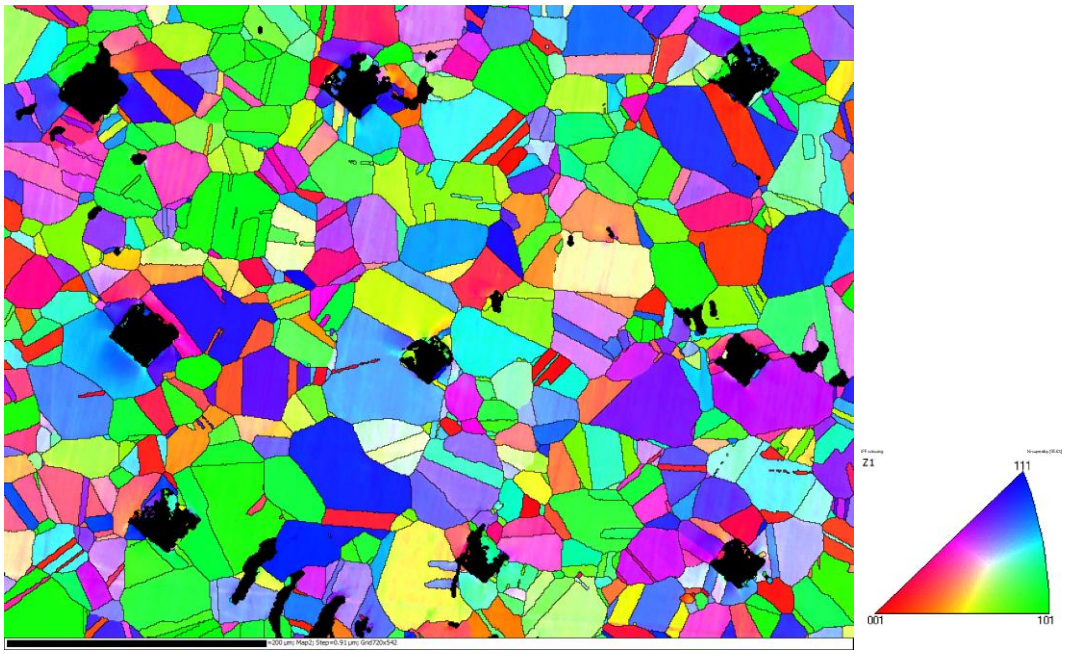

Figure 4.20: EBSD scan of pre-implanted marked Inconel X750.

Once this EBSD scan was obtained then the samples were implanted with helium ions and were then vacuum annealed to 700^{o}C. The samples were vacuum annealed to 700^{o}C because we had already found out that at 700^{o}C helium voids are accumulated at the grain boundary of the material. After implantation and vacuum annealing we tried to do EBSD scans on the same area

but no diffraction pattern was obtained because of the slight oxidation layer that was formed on the sample as a result we had to do SEM scans over this marked implanted vacuum annealed region to establish a relationship between helium voids accumulation and grain boundary misorientation.

The data from figure 4.19 was used to obtain the misorientation angle of the grain boundaries using the Oxford Instruments Channel 5 processing software which was then used to establish the relationship between helium void accumulation and grain boundary misorientation.

The EBSD map below is of the pre-implanted marked area of Inconel X750. The ten small white boxes correspond to the ten different areas which were scanned using SEM after implantation and vacuum annealing of the sample at 700^{o}C. These areas are studied individually for establishing a relationship between the concentration of voids and the misorientation angle.

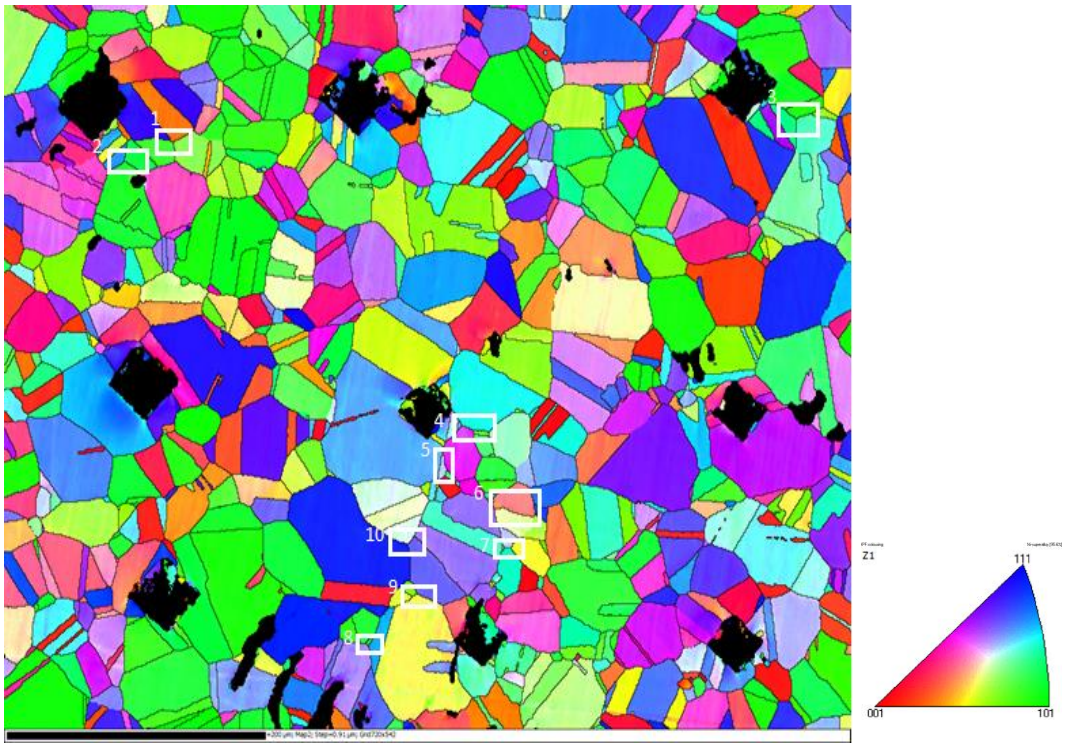

Figure 4.21: EBSD scan of pre-implanted marked Inconel X750 showing the areas used for establishing the relationship between the concentration of voids and misorientation angle

As discussed earlier, on account of slight oxidation, SEM scans were done after implanting and annealing the samples. Below are the various SEM images that were taken at the ten different

areas marked above. The lines and numbers in these SEM images have been used to refer to the different grain boundaries.

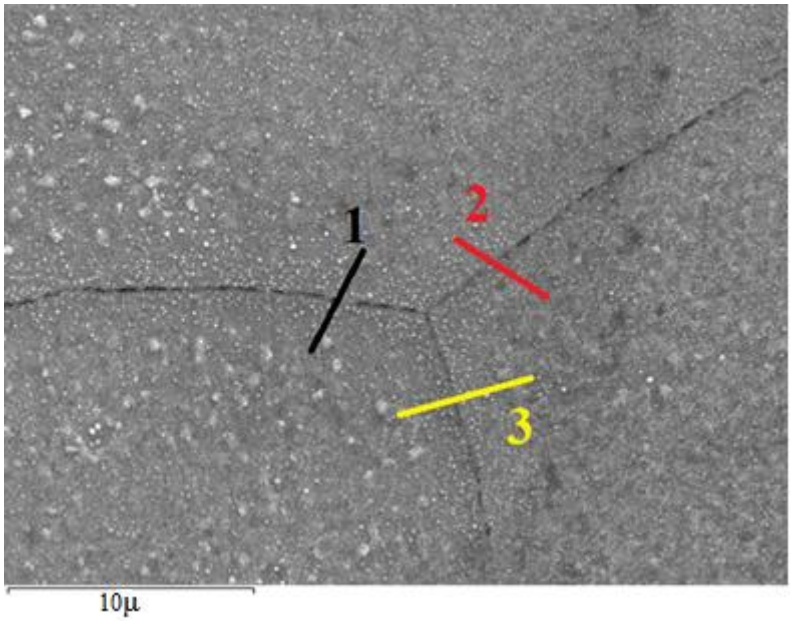

Misorientation angle for Grain Boundary 1: 31.2°
Misorientation angle for Grain Boundary 2: 46°
Misorientation angle for Grain Boundary 3: 28.1°

Figure 4.22: SEM Scan of Area 1

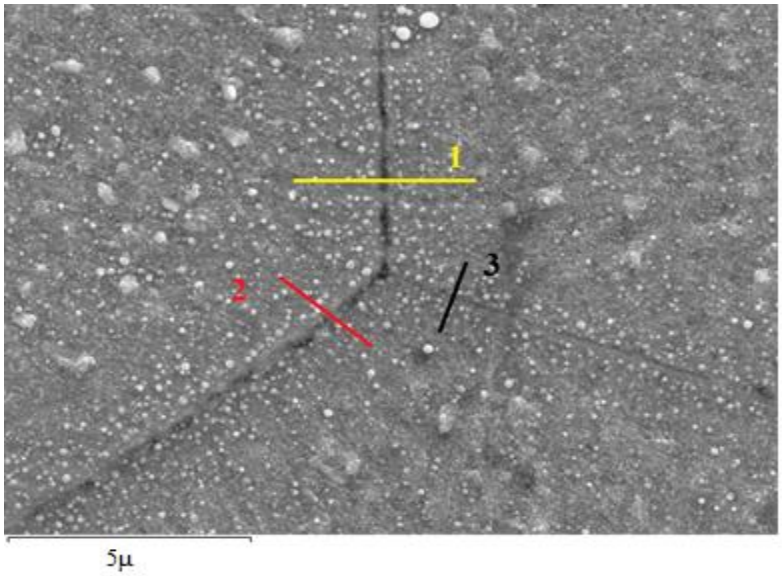

Misorientation angle for Grain Boundary 1: 30.7°
Misorientation angle for Grain Boundary 2: 51.7°
Misorientation angle for Grain Boundary 3: 15.1°

Figure 4.23: SEM Scan of Area 2

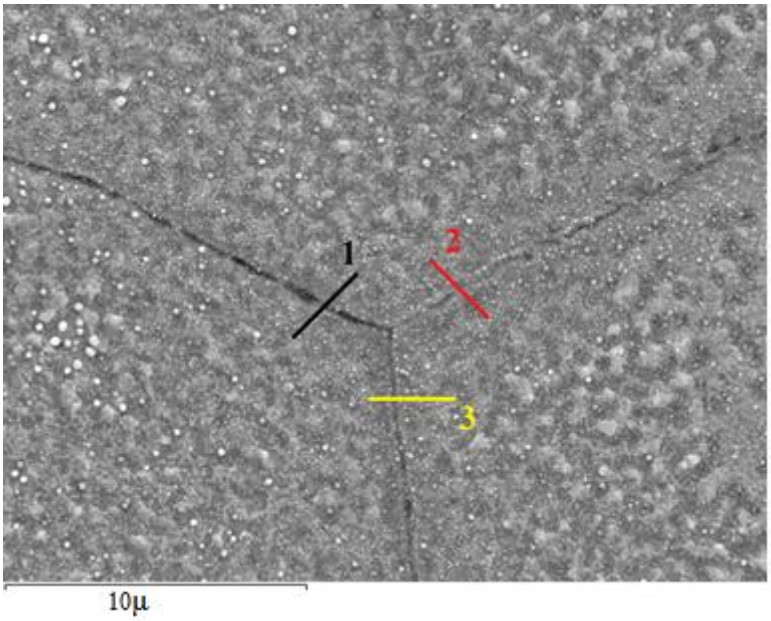

Misorientation angle for Grain Boundary 1: 47.2°
Misorientation angle for Grain Boundary 2: 27°
Misorientation angle for Grain Boundary 3: 28.1°

Figure 4.24: SEM Scan of Area 3

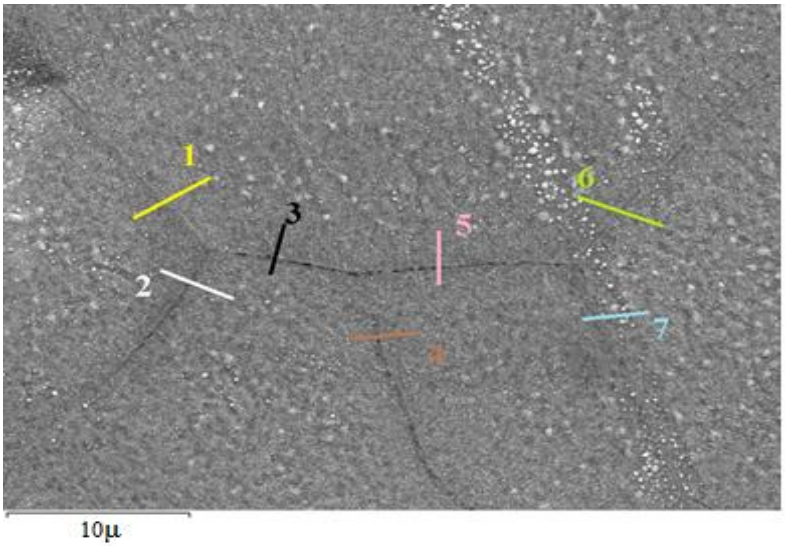

Misorientation angle for Grain Boundary 1: 10.5°
Misorientation angle for Grain Boundary 2: 39.5°
Misorientation angle for Grain Boundary 3: 49.6°
Misorientation angle for Grain Boundary 4: 40.2°
Misorientation angle for Grain Boundary 5: 48.8°
Misorientation angle for Grain Boundary 6: 28.1°
Misorientation angle for Grain Boundary 7: 15.5°

Figure 4.25: SEM Scan of Area 4

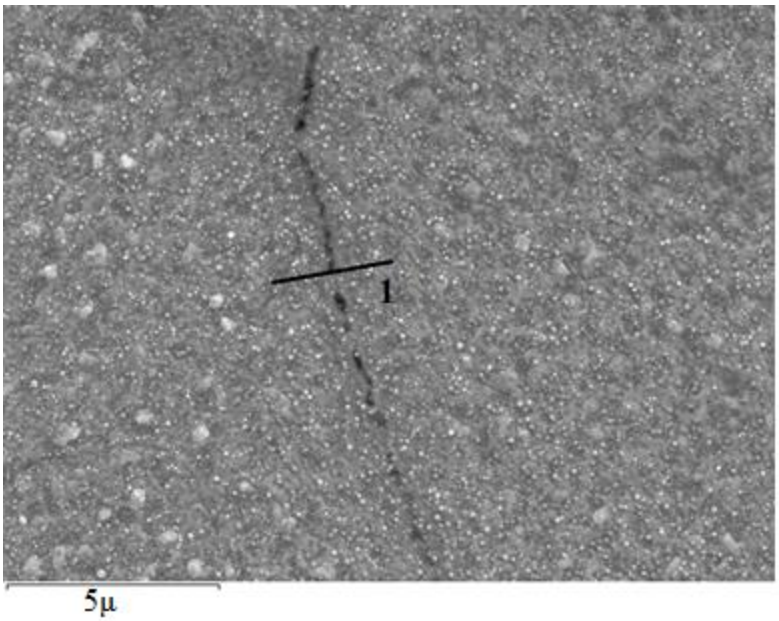

Misorientation angle for Grain Boundary 1: 39.5°

Figure 4.26: SEM Scan of Area 5

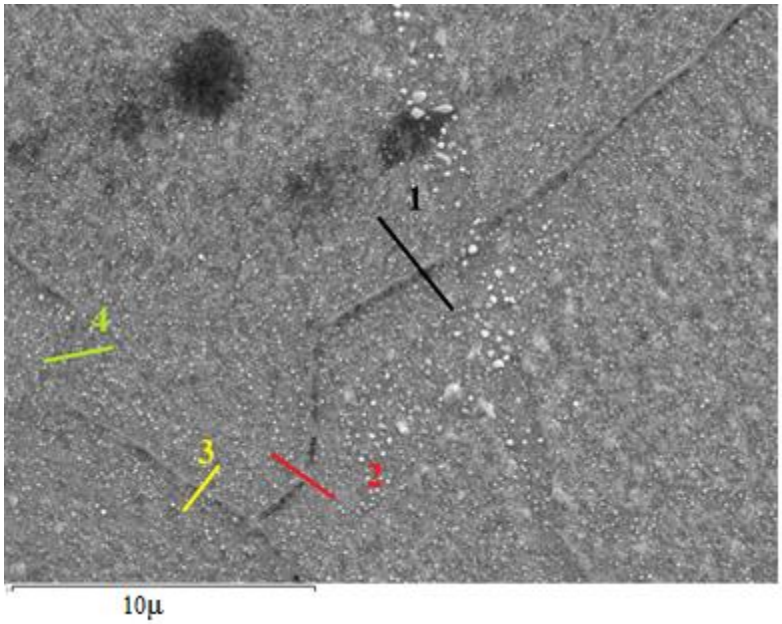

Misorientation angle for Grain Boundary 1: 33.2°
Misorientation angle for Grain Boundary 2: 47°
Misorientation angle for Grain Boundary 3: 43.5°
Misorientation angle for Grain Boundary 4: 17.5°

Figure 4.27: SEM Scan of Area 6

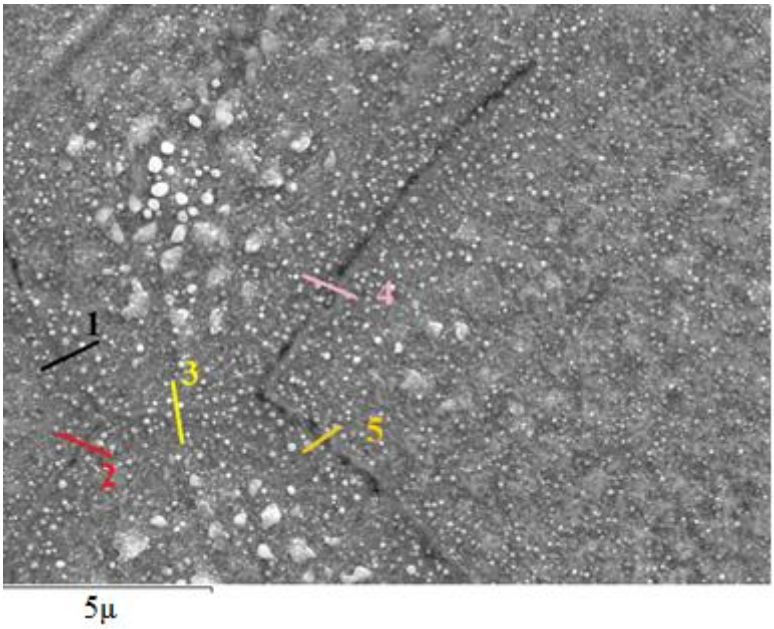

Misorientation angle for Grain Boundary 1: 40.5°
Misorientation angle for Grain Boundary 2: 54.5°
Misorientation angle for Grain Boundary 3: 17.6°
Misorientation angle for Grain Boundary 4: 38.2°
Misorientation angle for Grain Boundary 5: 46.9°

Figure 4.28: SEM Scan of Area 7

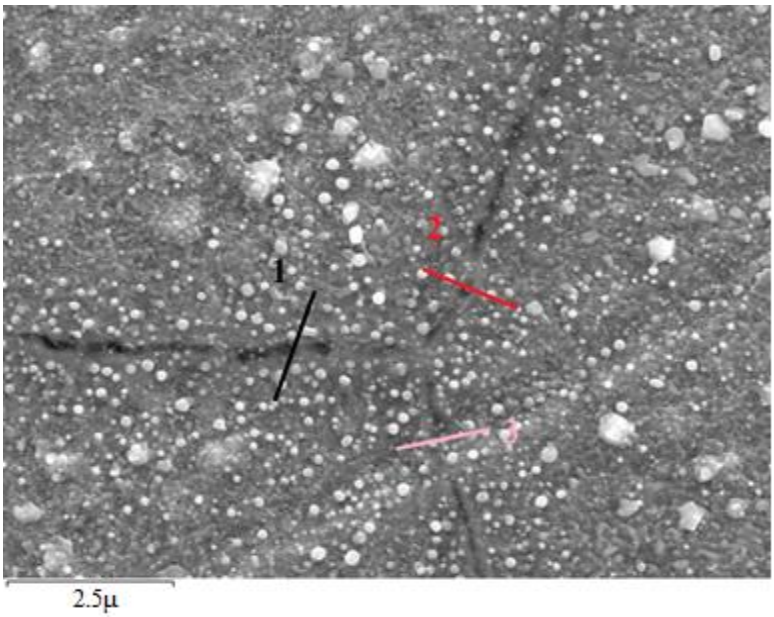

Misorientation angle for Grain Boundary 1: 47.5°
Misorientation angle for Grain Boundary 2: 38.6°
Misorientation angle for Grain Boundary 3: 28.1°

Figure 4.29: SEM Scan of Area 8

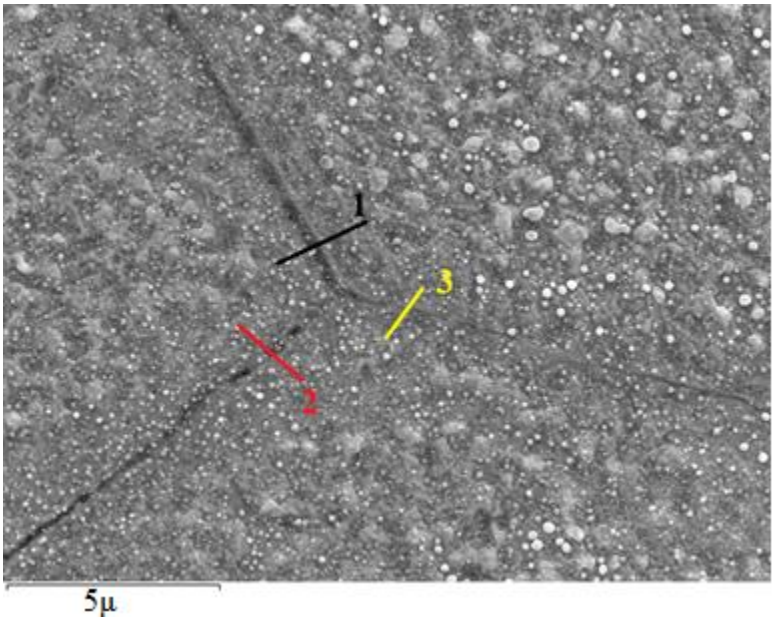

Misorientation angle for Grain Boundary 1: 36.3°
Misorientation angle for Grain Boundary 2: 46.5°
Misorientation angle for Grain Boundary 3: 55.1°

Figure 4.30: SEM Scan of Area 9

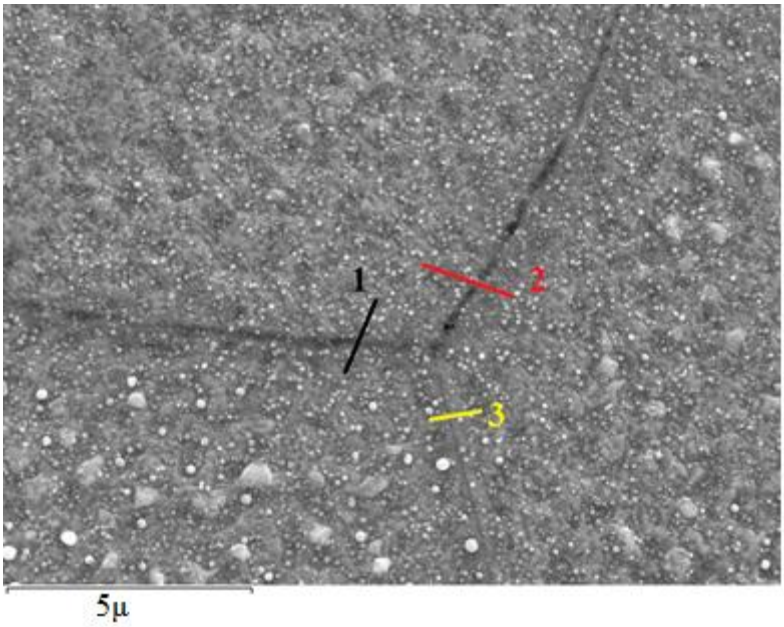

Misorientation angle for Grain Boundary 1: 33.1°
Misorientation angle for Grain Boundary 2: 44.6°
Misorientation angle for Grain Boundary 3: 29.8°

Figure 4.31: SEM Scan of Area 10

Similarly, as for Ni specimens the entire implanted area was observed under SEM and the length of each grain boundary and number of voids on each grain boundary were calculated. Figure 4.32 shows the misorientation profile of Inconel X750 sample. This figure was used to establish the relationship between the concentration of voids per micron and the misorientation angle.

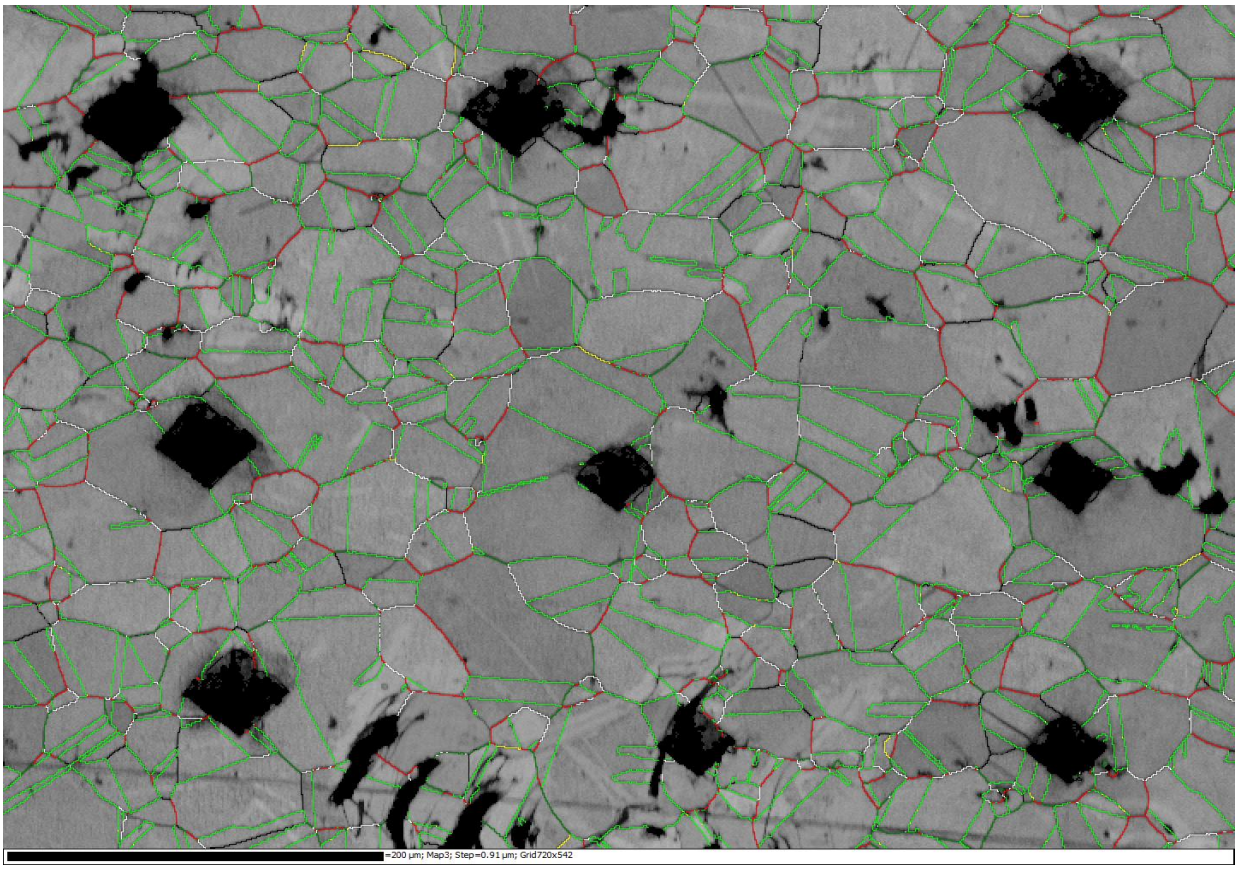

Misorientation Angle	Grain Boundary Color
>10	
>20	
>30	
>40	
>50	
>60	

Figure 4.32: The Misorientation angles for all the grain boundaries of Inconel X750

In order to obtain the relationship between helium void accumulation and grain boundary misorientation for Inconel X750 similar calculations were done as discussed in section 4.1.3 for pure Ni specimens.

Table 4.3: Concentration of voids per micron calculation for misorientation angle range 10° - 20° for Inconel X750.

Grain Boundary Misorientation (degree)	No. of Voids	Length of the Grain Boundary (micron)
10.5	24	30.69
12.25	24	20.32
12.32	22	30.65
14.25	15	23.36
14.38	29	45.98
14.96	15	20.36
15.16	11	19.65
15.26	26	39.62
15.26	20	30.65
15.32	22	27.69
15.5	20	30.69
15.55	13	17.58
15.69	32	37.25
16.25	8	15.25
16.98	12	24.65
17.36	15	27.62
17.5	25	45.68
17.51	19	30.65
17.56	21	48.36
17.58	13	29.65
17.6	9	24.32
18.69	24	35.96
19.39	23	52.36
19.57	25	40.69
19.63	8	20.69
19.69	5	19.69
Total	480	790.06
Concentration of voids per micron = 480/790.06 = 0.607549		

Table 4.3 shows the calculation of concentration of voids per micron for the misorientation angle range 10° - 20° for Inconel X750, similarly calculations were performed for grain boundaries range 0°-10°, 20°-30°, 30°-40°, 40°-50°, 50°-60° and 60°-70°. Table 4.4 and figure 4.33 summarizes these calculations. In table 4.4 it could be seen that the concentration of voids per micron increases from 0.61 ± 0.16 for a misorientation angle range 0°-10° to 1.16 ± 0.16 for a misorientation angle range 60°-70°.

Table 4.4: Calculated concentration of voids per micron for Inconel X750.

Misorientation angle range	Concentration of voids per micron
0°-10°	0 ± 0.16
10°-20°	0.61 ± 0.16
20°-30°	0.91 ± 0.16
30°-40°	1.05 ± 0.16
40°-50°	1.09 ± 0.16
50°-60°	1.11 ± 0.16
60°-70°	1.16 ± 0.16

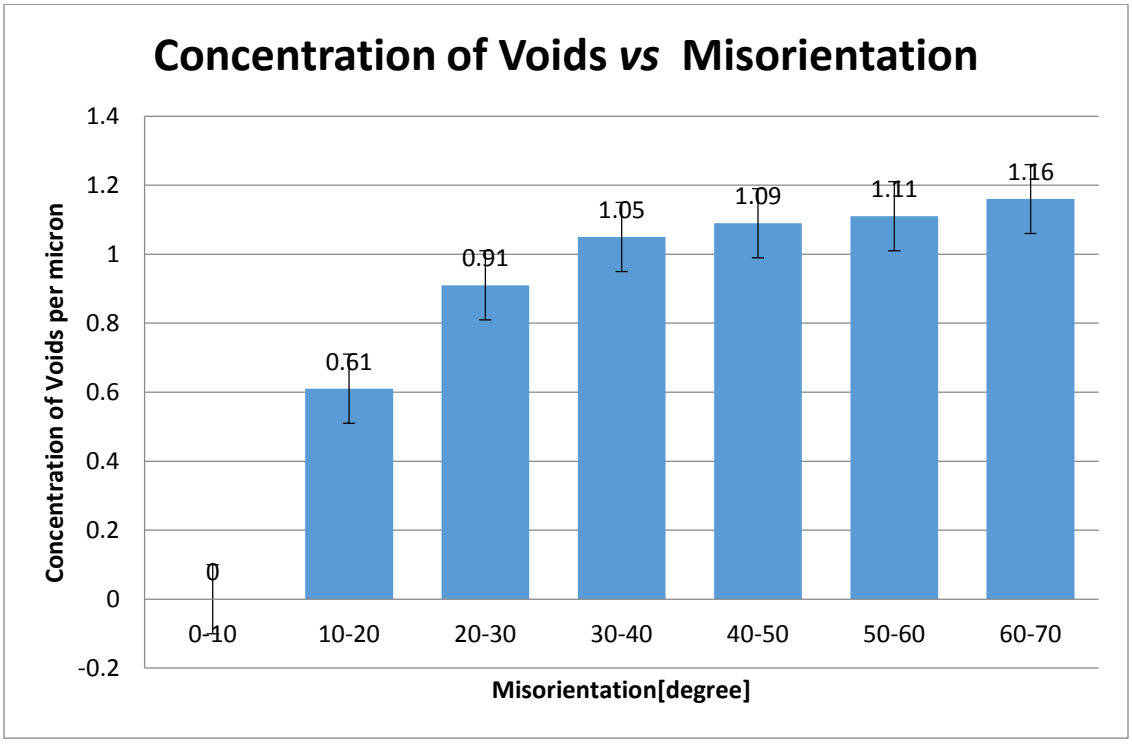

Figure 4.33: Concentration of voids per micron vs misorientation angle for Inconel X750.

It can be clearly observed from the graph that the concentration of voids per micron is increasing with an increase in the misorientation angle. This is because the energy of grain boundary increases with an increase of the misorientation angle thus giving more free volume to the voids to form and accumulate. It can be clearly seen from figure 4.17 that the grain boundary energy is proportional to the volume expansion for pure Ni. It means that at a higher energy grain boundary there would be more free volume thus more space would be available for the helium voids to accumulate. Figure 4.17 is taken into consideration here because from figure 4.19 and table 3.1 we can see that Inconel X750 contains approximately 70 wt% Ni. Therefore, the behaviour of Inconel X750 alloy would be similar to that of pure Ni. To conclude we can say that a high angle grain boundary would have higher concentration of voids as compared to a low angle grain boundary.

Table 4.5 and figure 4.34 summarizes the results obtained (from table 4.2 and table 4.4)

Table 4.5: Concentration of voids per micron for Inconel X750 and Pure Ni.

Misorientation angle range	**Concentration of voids per micron**	
	Inconel X750	**Pure Ni**
0°-10°	0 ± 0.16	0 ± 0.16
10°-20°	0.61 ± 0.16	0.63 ± 0.16
20°-30°	0.91 ± 0.16	0.94 ± 0.16
30°-40°	1.05 ± 0.16	1.07 ± 0.16
40°-50°	1.09 ± 0.16	1.11 ± 0.16
50°-60°	1.11 ± 0.16	1.12 ± 0.16
60°-70°	1.16 ± 0.16	1.19 ± 0.16

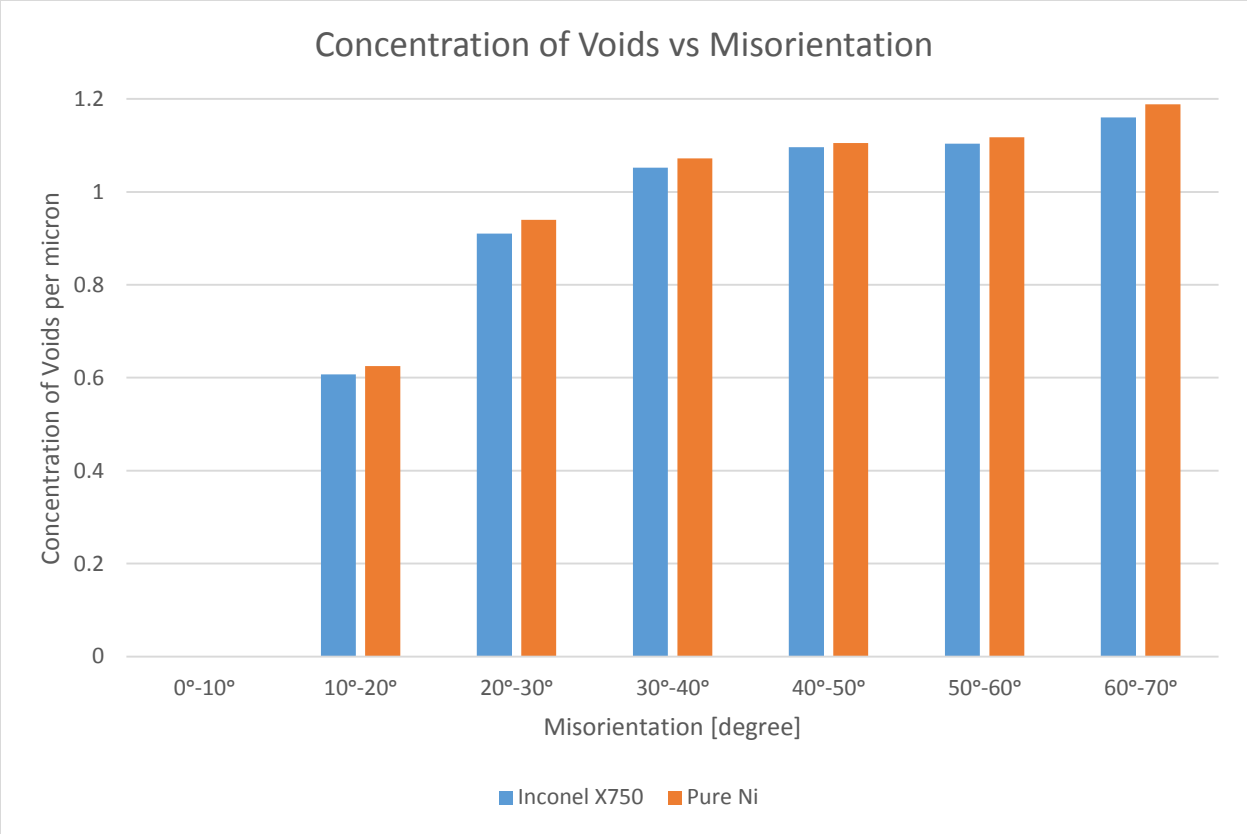

Figure 4.34: Concentration of voids vs misorientation for Inconel X750 and pure Ni.

It could be clearly seen from table 4.5 and figure 4.34 that for both materials (Pure Ni and Inconel X750) the concentration of voids per micron increases with an increase in the misorientation angle. In figure 4.34 a similar trend could be seen for pure Ni and Inconel X750 alloy because the Inconel X750 alloy has around 70% Nickel, therefore its behavior is very similar to pure Ni.

CHAPTER FIVE

CONCLUSIONS AND FUTURE WORK

For this project, pure Ni and Inconel X750 alloy were subjected to various tests in order to evaluate the location of He voids. The implantation parameters were thoroughly cross checked to standardize the implantation process. SEM and EBSD imaging were done on a large number of samples in order to establish a relationship between annealing temperatures and helium void accumulation. More than hundred different grain boundaries were investigated for each of the materials (pure Ni and Inconel X750 alloy) in order to carry out statistical studies and establish a relationship between helium void accumulation and grain boundary misorientation. Based on the various tests carried out the following conclusions could be drawn:

1. We demonstrated that Tandem accelerator could be used for Helium ion implantation which made it possible for us to observe helium voids formed in the implanted samples.
2. With the help of SEM analysis we established a relationship between annealing temperature and formation of voids, thus concluded that the diffusion of helium voids increases with an increase in annealing temperature.
3. TEM, EDS and SEM analysis of implanted pure Ni and Inconel X750 samples vacuum annealed to 700^{o}C confirmed the presence of helium voids predominantly at high angle grain boundaries.
4. We also conclude that the concentration of voids per micron increases with an increase in the misorientation angle as the energy of grain boundary increases with an increase in the misorientation angle.

5.1 Recommendations for future work

1. Microhardness tests should also be carried out on implanted and annealed materials in order to establish a relationship between implantation and hardness.
2. In-situ failure analysis should also be done to get a better understanding of the effect of grain boundary misorientation on crack nucleation and propagation.

REFERENCES

1. *Climate Change 2013: The Physical Science Basis* (Rep.). (2013). Intergovernmental Panel on Climate Change. Retrieved April 3, 2016

2. *World Energy Outlook 2013* (Rep.). (2013). International Energy Agency. Retrieved April 3, 2016.

3. World Energy Needs and Nuclear Power. Retrieved April 03, 2016, from http://www.world-nuclear.org/information-library/current-and-future-generation/world-energy-needs-and-nuclear-power.aspx

4. Energy Sources and Distribution. Retrieved April 03, 2016, from http://www.nrcan.gc.ca/energy/uranium-nuclear/7695

5. Rowcliffe, A., Mansur, L., Hoelzer, D., & Nanstad, R. (2009). Perspectives on radiation effects in nickel-base alloys for applications in advanced reactors. *Journal of Nuclear Materials, 392*(2), 341-352. doi:10.1016/j.jnucmat.2009.03.023

6. Griffiths, M. (2013). The Effect of Irradiation on Ni-containing Components in CANDU Reactor Cores: A Review. *AECL Nuclear Review, 2*(2), 89-89. doi:10.12943/anr.2013.0001

7. CANDU Reactors. Retrieved April 03, 2016, from http://www.candu.org/candu_reactors.html

8. Garland, W. J. *How and Why is CANDU designed the way it is* (Rep.). Retrieved April 9, 2016, from http://www.candu.org/pdf/how_reactor_works.pdf

9. CANDU technology - Canadian Nuclear Association. Retrieved April 09, 2016, from https://cna.ca/technology/energy/candu-technology/

10. Ahmad, M. M. (2011). *Transmutation rates in the annulus gas of pressure tube water reactors*. University of Ontario Institute of Technology. Retrieved from http://hdl.handle.net/10155/182

11. *Enhanced CANDU 6 Technical Summary* (Rep.). Retrieved April 9, 2016, from Candu Energy Inc. website: http://www.candu.com/site/media/Parent/EC6__Technical Summary_2012-04.pdf

12. Walters L.C., Williams A.F., CANDU Fuel Bundle Deformation Model, 2004 International ANSYS Conference 52.

13. Azevedo, C. (2011). Selection of fuel cladding material for nuclear fission reactors. *Engineering Failure Analysis, 18*(8), 1943-1962. doi:10.1016/j.engfailanal.2011.06.010

14. *A Technology Roadmap for Generation IV Nuclear Energy Systems* (Rep.). (2002). U.S. DOE Nuclear Energy Research Advisory Committee and the Generation IV International Forum. Retrieved April 3, 2016.

15. Greenwood, L., & Garner, F. (1996). Hydrogen generation arising from the ^{59}Ni(n, p) reaction and its impact on fission—fusion correlations. *Journal of Nuclear Materials, 233-237*, 1530-1534. doi:10.1016/s0022-3115(96)00264-4

16. Greenwood, L. (1983). A new calculation of thermal neutron damage and helium production in nickel. *Journal of Nuclear Materials, 115*(2-3), 137-142. doi:10.1016/0022-3115(83)90302-1

17. Colin, J. D. (2015). *The Effects of Irradiation on Inconel X-750*. McMaster University. Retrieved April 9, 2016, from http://hdl.handle.net/11375/18091

18. Adams, J., & Wolfer, W. (1989). Formation energies of helium-void complexes in nickel. *Journal of Nuclear Materials, 166*(3), 235-242. doi:10.1016/0022-3115(89)90220-1

19. Yang, L., Zu, X., & Gao, F. (2008). Ab initio study of formation, migration and binding properties of helium–vacancy clusters in aluminum. *Physica B: Condensed Matter, 403*(17), 2719-2724. doi:10.1016/j.physb.2008.02.015

20. Chauhan, A.K., Szpunar, J.A., Szpunar, B., Bradley, M.P., Saini, V.K., Griffiths, M., & Chicoine, M. (2015, August). *Helium Based Degradation of Nickel Superalloys.* Paper presented at the 3rd International Conference on Manufacturing Engineering and Technology for Manufacturing Growth, Vancouver, Canada. ISBN:978-1-61275-074-3, IERI & PRESS, 178-181.

21. Greenwood, L., & Smither, R. (1985). SPECTER: Neutron damage calculations for materials irradiations. doi:10.2172/6022143

22. Saini, V. K. (2014). *Helium and Hydrogen production in Ni based alloys for generation IV nuclear reactors* (Rep.).

23. Inconel alloy X750 - Special Metals. Retrieved April 9, 2016, from http://www.specialmetals.com/assets/documents/alloys/inconel/inconel-alloy-x-750.pdf

24. S R I M. Retrieved April 09, 2016, from http://www.srim.org/SRIM/SRIMINTRO.htm

25. CCPAC facilities. Retrieved April 09, 2016, from http://ion.lps.umontreal.ca/facilities.html

26. Matossian, J. N. (1994). Plasma ion implantation technology at Hughes Research Laboratories. *J. Vac. Sci. Technol. B Journal of Vacuum Science & Technology B: Microelectronics and Nanometer Structures*, *12*(2), 850-853. doi:10.1116/1.587358

27. CanmetMATERIALS. Retrieved April 09, 2016, from http://www.nrcan.gc.ca/mining-materials/materials-technology/8234

28. Garner, F., Hamilton, M., Simons, R., & Maxon, M. (1991). Isotopic tailoring with 59Ni to study the influence of helium/dpa ratio on tensile property changes. *Journal of Nuclear Materials*, *179-181*, 554-557. doi:10.1016/0022-3115(91)90148-z

29. Garner, F., Greenwood, L., & Oliver, B. (n.d.). A Reevaluation of Helium/dpa and Hydrogen/dpa Ratios for Fast Reactor and Thermal Reactor Data Used in Fission-Fusion Correlations. *Effects of Radiation on Materials: 18th International Symposium*. doi:10.1520/stp13904s

30. Garner, F., Oliver, B., & Greenwood, L. (1998). The dependence of helium generation rate on nickel content of Fe–Cr–Ni alloys irradiated to high dpa levels in EBR-II. *Journal of Nuclear Materials*, *258-263*, 1740-1744. doi:10.1016/s0022-3115(98)00297-9

31. Lu, J. (1995). *Computer modeling of intergranular fracture in textured materials* (Unpublished master's thesis). McGill University. Retrieved from http://digitool.Library.McGill.CA:80/R/-?func=dbin-jump-full&object_id=39950&silo_library=GEN01

APPENDIX

Copyright Permissions

Chapter 2:
Figure 2.3, Figure 2.4 and Figure 2.5

4/13/2016 CNL Nuclear Review
http://pubs.cnl.ca/page/cnr-about/permissions

Permissions

Copyright Permission Policy

These guidelines apply to the reuse of articles, figures, charts and photos in *CNL Nuclear Review*.

For authors reusing their own material:

Authors need NOT contact the journal to obtain rights to reuse their own material. They are automatically granted permission to do the following:
Reuse the article in print collections of their own writing.
Present a work orally in its entirety.
Use an article in a thesis and/or dissertation.
Reproduce an article for use in the author's courses. (If the author is employed by an academic institution, that institution also may reproduce the article for teaching purposes.)
Reuse a figure, photo and/or table in future commercial and noncommercial works.
Post a copy of the paper in PDF.
Link to the journal site containing the final edited PDFs created by the publisher.

Please note that authors must include the following citation when using material that appeared in *CNL Nuclear Review*:

"This research was originally published in CNL Nuclear Review Author(s), Year, Title. Journal Name. Vol, Issue. "

For other parties using material for noncommercial use:

Other parties are welcome to copy, distribute, transmit and adapt the work — at no cost and without permission — for noncommercial use as long as they attribute the work to the original source using the citation above.

Examples of noncommercial use include:

Reproducing a figure for educational purposes, such as assignments, essays, coursework or lecture presentations, with attribution.
Appending a reprinted article to a Ph.D. dissertation, with attribution.

Chapter 4:
Figure 4.17

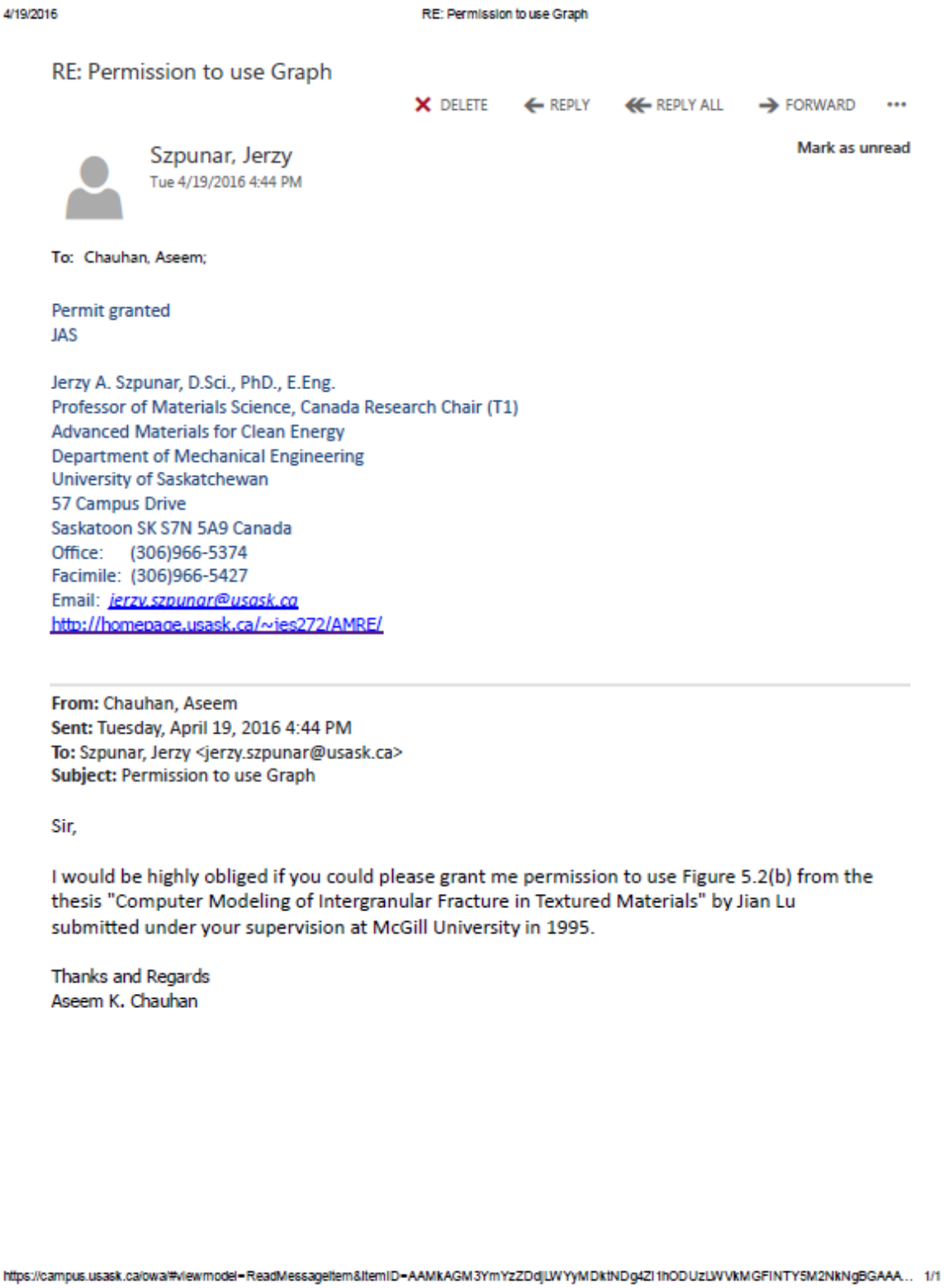

4/19/2016 RE: Permission to use Graph

RE: Permission to use Graph

DELETE REPLY REPLY ALL FORWARD ...

Mark as unread

Szpunar, Jerzy
Tue 4/19/2016 4:44 PM

To: Chauhan, Aseem;

Permit granted
JAS

Jerzy A. Szpunar, D.Sci., PhD., E.Eng.
Professor of Materials Science, Canada Research Chair (T1)
Advanced Materials for Clean Energy
Department of Mechanical Engineering
University of Saskatchewan
57 Campus Drive
Saskatoon SK S7N 5A9 Canada
Office: (306)966-5374
Facimile: (306)966-5427
Email: jerzy.szpunar@usask.ca
http://homepage.usask.ca/~jes272/AMRE/

From: Chauhan, Aseem
Sent: Tuesday, April 19, 2016 4:44 PM
To: Szpunar, Jerzy <jerzy.szpunar@usask.ca>
Subject: Permission to use Graph

Sir,

I would be highly obliged if you could please grant me permission to use Figure 5.2(b) from the thesis "Computer Modeling of Intergranular Fracture in Textured Materials" by Jian Lu submitted under your supervision at McGill University in 1995.

Thanks and Regards
Aseem K. Chauhan

https://campus.usask.ca/owa/#viewmodel=ReadMessageItem&ItemID=AAMkAGM3YmYzZDdjLWYyMDktNDg4ZI1hODUzLWVkMGFlNTY5M2NkNgBGAAA... 1/1